Universidade de Aveiro Departamento de Física,
2013

Pedro Manuel Mendes Correia

Estudos de detetores gasosos de radiação: GEM, THGEM e Câmara Compton

Studies in gaseous radiation detectors: GEM, THGEM and Compton Camera

Universidade de Aveiro Departamento de Física,
2013

Pedro Manuel Mendes Correia

Estudos de detetores gasosos de radiação: GEM, THGEM e Câmara Compton

Studies in gaseous radiation detectors: GEM, THGEM and Compton Camera

"If I have seen further it is by standing on ye sholders of Giants"

— Sir Isaac Newton

Pedro Manuel Mendes Correia

Estudos de detetores gasosos de radiação: GEM, THGEM e Câmara Compton

Studies in gaseous radiation detectors: GEM, THGEM and Compton Camera

Tese apresentada à Universidade de Aveiro para cumprimento dos requesitos necessários à obtenção do grau de Mestre em Engenharia Física, realizada sob a orientação científica do Doutor João Filipe Calapez de Albuquerque Veloso, Professor do Departamento de Física da Universidade de Aveiro

Este trabalho foi financiado pelo projecto "Desenvolvimento de foto-detetores para leitura em detetores RICH" PTDC/FIS/110925/2009

o júri / the jury

presidente / president

Doutora Teresa Maria Fernandes Rodrigues Cabral Monteiro
Professora Associada com Agregação da Universidade de Aveiro

Doutor Joaquim Marques Ferreira dos Santos
Professor Catedrático da Universidade de Coimbra

Doutor João Filipe Calapez de Albuquerque Veloso
Professor Auxiliar da Universidade de Aveiro (orientador)

agradecimentos / acknowledgements

Aos meus pais, António e Fátima, às Saras, e à restante família pela ajuda e apoio durante estes 5 anos.

Aos Professor João Veloso, pela oportunidade de desenvolver as minhas capacidades no grupo de DRIM da Universidade de Aveiro e por toda a ajuda dada ao longo do trabalho.

Aos membros do grupo DRIM da Universidade de Aveiro, especialmente ao Cacia, ao Arouca, à Ana Luísa, ao Lipe, à Lara, ao Fábio, ao Carlitos, à Anabela, ao Moutinho e ao Tiago, pelos momentos de trabalho, ajuda e camaradagem.

Aos meus amigos mais próximos durante o curso, especialmente ao Fábio, ao Prezas, ao Anselmo, ao Xuxa, ao Santiago, ao Amorim, ao André e ao Marco, bem como a todos os membros do grupo Oldschool.

Ao Professor Filipe e ao Professor Vale, por me terem incutido o gosto pela Física e Matemática em geral.

Ao Professor Ricardo Dias por toda a ajuda durante os primeiros anos do curso e por toda a disponibilidade posterior.

Ao Rob Veenhof e Mythra Nemallapudi, pela importante ajuda no desenvolvimento e correcção de software utilizado ao longo desta tese, e nos resultados experimentais obtidos com GEMs.

À equipa de futsal de Engenharia Física, por me ajudarem a manter a forma física e a disposição necessárias ao bom ambiente de trabalho.

Palavras-Chave Deriva de electrões, avalanches de electrões, detetores gasosos de radiação, acumulação de carga, electroluminescência

Resumo

O conhecimento dos fenómenos associados à deriva de cargas em meios gasosos, especialmente electrões, assume extrema importância para o estudo e compreensão de detetores gasosos de radiação.

Ao longo deste trabalho, dois tipos de detetores gasosos foram estudados, os detetores gasosos microestruturados (MPGD) e um novo tipo de Câmara γ especialmente desenvolvida para deteçao de eventos Compton, que usa um meio gasoso como meio de deteção, designada de Câmara Compton gasosa.

A simulação da operação de dois MPGD, o GEM e o THGEM, incidiu no estudo do efeito de acumulação de carga no detetor (*charging-up*), bem como no estudo da importância de determinados parametros geométricos dos detetores para o ganho em carga de ambos. Medidas experimentais da acumulação de carga no THGEM foram feitas e comparadas com resultados experimentais.

Relativamente à Camara Compton, fez-se a simulação da deriva de eletrões primários na região de absorção e cintilação tendo em vista tirar conclusões acerca do gás mais apropriado para a deteção e avaliar o desempenho do detetor na determinação da posição e energia depositada em cada interação dos raios γ.

Keywords Electron drift, electron avalanches, radiation gaseous detectors, charging-up, electroluminescence.

Abstract The understanding of the physical behaviour of the drift of charged particles inside a gas, specially electrons, is vital for the study and comprehension of gaseous radiation detectors.
During this work, two types of gaseous detectors were studied, the micropattern gaseous detectors (MPGD) and a new type of γ Camara developed for the Compton events detection, called Compton Camera, that uses a gas vessel as an absorption medium.
Simulation of the operation of two MPGD, the GEM and the THGEM were made, focused in the study of the charging-up effect in the detectors, and also in the study of the influence of certain geometric parameters for the performance of the detectors. Experimental measurements in THGEM were made and compared with simulation results.
For the Compton Camera, the simulation of the drift of electrons in the gas media was made to decide which is the best gas choice and to evaluate the performance of the detector for the position and deposited energy determination of each γ-ray interaction.

Contents

List of Figures

List of Tables

List of Acronyms

MWPC Multi-wire proportional counter

MSGC Micro Strip Gas Chamber

MPGD Micro-Pattern Gaseous Detector

GEM Gas electron multiplier

THGEM Thick Gas electron multiplier

MHSP Micro-Hole and Strip Plate

VUV Vacuum Ultraviolet

VIS-IR Visible to Infra-Red

$\boldsymbol{Y}_{VUV}$ Scintillation yield of VUV

$\boldsymbol{Y}_{VIS-IR}$ Scintillation yield of VIS-IR

FEM Finite Element Methods

neBEM Nearly Exact Bondary Element Methods

RD51 Collaboration Research & Development of Micro-Pattern Gas Detectors

THCOBRA Thick-COBRA or Thick-MHSP with a patterned electrode

CsI Cesium Iodide

Publications and Communications

Publications in International Journals

"Simulation of VUV electroluminescence in micropattern gaseous detectors: the case of GEM and MHSP" Authors: Carlos Oliveira, **P. M. M. Correia**, H. Schiendler, António Ferreira, C. M. B. Monteiro, J. M. F. dos Santos, S. Biagi, R. Veenhof, J. F. C. A. Veloso Journal of Instrumentation Volume 7, 2012, P09006

"Simulation of gaseous Ar and Xe electroluminescence in the Near Infra-Red range" Authors: Carlos Oliveira, **Pedro M. M. Correia**, António Ferreira, S. Biagi, R. Veenhof, J. Veloso Nuclear Instruments and Methods in Physics Research Section A Volume 722,2013, Pages 14

"A Gaseous Compton Camera using a 2D-sensitive gaseous photomultiplier for Nuclear Medical Imaging" Authors: C.D.R. Azevedo, , F.A. Pereira, T. Lopes, **P.M.M. Correia**, A.L.M. Silva, L.F.N.D. Carramate, D.S. Covita, J.F.C.A. Veloso Nuclear Instruments and Methods in Physics Research Section A, Available online 25 May 2013

Oral Communications

"Charging-up studies: the case of GEM and THGEM" **P.M.M.Correia**, C. Oliveira, C. D. R. Azevedo, J. F. C. A. Veloso, R. Veenhof RD51 Collaboration meeting; 5-6 Jully, 2013, Zaragoza University, Spain

"CT System With Energy Resolving Capability using a THCOBRA based Detector"; L. F. N. D. Carramate, C. D. R. Azevedo, A. L. M. Silva, T. Lopes, **P. Correia**, I. F. Castro, A. M. da Silva and J. F. C. A. Veloso; 15th International Workshop on Radiation Imaging Detectors; 24-27 June 2013, Paris, France

"Improved efficiency in charging up calculations" **P.M.M.Correia**, C. Oliveira, J. F. C. A. Veloso, R. Veenhof RD51 Mini-Week 30 January - 1 February 2013, CERN, Switzerland "How to simulate thick GEM charging"

P.M.M.Correia, C. Oliveira,J. F. C. A. Veloso, R. Veenhof RD51 Mini-Week 3-5 December 2012, CERN,Switzerland "GEM and THGEM charging up calculations"

P.M.M.Correia, C. Oliveira,J. F. C. A. Veloso, R. Veenhof RD51 Mini-Week 30 September-5 October, Stony Brook University, United States of America. "Gas gain in single GEM: Charging-up effect at different voltages"

Posters

"Charging-up studies: the case of GEM and THGEM" **P.M.M.Correia**, C. Oliveira,C. D. R. Azevedo,J. F. C. A. Veloso, R. Veenhof, MPGD 2013; 1-4 Jully, 2013, Zaragoza University, Spain

Chapter 1

Introduction

In the late 19th century, relevant studies lead to the discovery of new types of radiation.

The discovery of the X-ray radiation by William Roentgen in 1895[1], followed in the next year by the discovery of the radioactive decay, with radiation emission, first reported by Henri Becquerel[2], were probably the trigger for the research in this subject at that time.

Since these new types of radiation are invisible to our eyes, as we know today, the only way to detect the existence of this radiation is by indirect detection. Roentgen was the first person to observe X-rays in a luminescent material, and after some time he made the world's first radiography, when he irradiated a photographic plate sensible to X-rays revealing part of the plate.

In early 20^{th} century, the research evolution lead to new ways of detecting radiation. The use of ionizable materials to detect radiation (e.g. gases) became more frequent. Thompson won a Nobel Prize in 1906 for his study of the electrical conductivity of ionized gases[3], and Victor Hess was probably the first to use a gaseous ionizable medium to detect radiation in 1910, when he found the first evidence for the existence of cosmic rays[4].

Some years later, Geiger and Mueller developed the so called Geiger-Mueller counter, a device that counts the number of interactions between gas particles and ionizing radiation[5]. The evolution of gaseous detectors lead to the development of the multi-wire proportional chamber (MWPC) by Charpak, who won the Noble Prize in Physics in 1992[6]. The MWPC represented a new world of possibilities in radiation detection, because it combined the prior knowledge of gaseous detectors with recent discoveries (at that time) concerning integrated electronic circuits and computed signal analysis.

In 1988, a new device was introduced to the scientific community, the Micro Strip Gas Chamber (MSGC) [7], which combines the use of an ionizable gaseous medium with recent technologies of production and assembly of micro pattern electronic devices. This marks the birth of the Micro Pattern Gaseous Detectors (MPGDs).

Due to the evolution of technology, two new important MPGDs emerged, the Micromegas (developed in 1996 by Ioannis Giomataris[8]) and the Gas Electron Multiplier (GEM, developed in 1997 by Fabio Sauli[9]). The innovation of these two designs is related to the facility of manufacturing, the relative operational stability, the reduced size and the better performances for particle tracking applications, compared with

older technology. More recent detectors like THGEM[10], Micro-Hole and Strip Plate (MHSP)[11] and InGrid[12] were developed based in the previous existent MPGDs.

Parallel to the development of gaseous detectors, solid state detectors have also been in development. Although the basic technology has more than 100 years, the use of the new generation of gaseous detectors is preferable in some situations, due to some important advantages of gaseous detectors when compared with recent solid state detectors: solid state devices have small detection areas, they are very expensive for larger areas while gaseous detectors are cheaper, and larger gaseous detectors can be built with less effort.

In this work we studied two types of gaseous detectors. Part of this work includes the study and measurement of some operational properties of two MPGDs (the GEM and THGEM), while the other part covers the study and simulation of a new γ-camera, the so-called Compton Camera, which is being developed by our group and which uses electronic collimation for γ rays detection instead of mechanical collimation.

Regarding the MPGDs, an intensive study of the charging-up effect, that occurs in detectors with insulator surfaces exposed to the gas media, was carried out, presenting two methods to simulate this effect and comparing them with several experimental measurements. The variation of some geometric parameters of these detectors was studied in order to investigate their influence in the response of the detectors.

Regarding the study of the Compton Camera, the first studies in the electromagnetic configuration of the detector were performed. The electric field and the drift of charges inside the detector were simulated, and the drift velocity of electrons for various gases and gas mixtures was calculated. The response of the detector in the determination of the interaction position of the radiation in the gas and the energy deposited by the interacting radiation was evaluated.

Chapter 2

Gaseous detectors

A gaseous detector consists of a chamber filled with a gas, in which incoming ionizing particles like X or γ rays can interact with the gas particles and deposit energy. Normally noble gases or mixtures containing them are used, because noble gases are inert, so they do not react chemically with other materials in the detector, and they are not electronegative, which means that electrons will not tend to combine with gas particles, reducing detection efficiencies.

When an incoming particle passes through the gas, it can interact with its particles and deposit part or all the carried energy. As a consequence of the interaction, excitations or ionizations may occur. Depending on the potentials applied to the detector, it can detect the deposited energy and/or the number of interacting particles in the gas, by collecting electrons or photons produced during the interaction.

A simple detector is exemplified in Fig. 2.1.

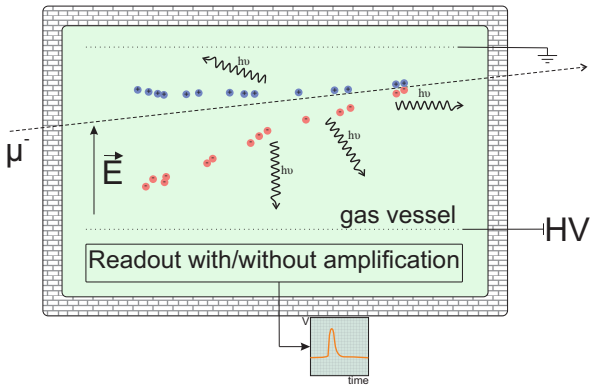

Figure 2.1: An incoming particle (muon μ^-, for example) interacts in the gas media, transferring part of its energy to gas particles along its path. A trail of ions, electrons and photons is created during several interactions with gas particles. An amplification stage can be used before electronic and/or lighting signal readout.

2.1 Interaction of photons with matter

The interaction of radiation with matter can occur in three different ways. The incident photon can be absorbed by the material, and deposit all its energy to the

medium, can be scattered, loosing part of the energy to the medium, by pair production, if the energy of the photon is sufficient high. When a photon is absorbed or scattered, we say that it was attenuated.

Radiation can be divided into *ionizing* and *non-ionizing* radiation, depending on the carried energy. Ionizing radiation is the radiation with enough energy to ionize matter. Since the ionization energy of hydrogen atom is about 13.6 eV, is usual to define a threshold near 10 eV to distinguish between ionizing (above 10 eV) and non-ionizing (bellow 10 eV) radiation.

Charged particles, such as accelerated electrons, protons and atomic nuclei are said to be directly ionizing radiation because they can eject shell electrons directly through charged-particle interactions. Neutrons, X and γ rays are called indirect ionizing radiation, because they don't have electric charge. For our discussion, we will focus in the interactions of electrons, ions, X and γ rays with matter.

Interactions between X and γ-rays and matter can be distinguished in photoelectric absorption, coherent (or Rayleight) scattering, incoherent (or Compton) scattering, and pair production.

2.1.1 Photoelectric absorption

The total energy of the incoming photon can be transferred only in one interaction to a shell electron. The kinetic energy of the removed electron is given by 2.1

$$K = h\nu - W \tag{2.1}$$

where K is the kinetic energy of the removed electron, $h\nu$ is the energy of the incident photon, and W is the work function of the removed electron, depending on which shell the electron was.

If an inner shell electron is ejected and leaves a vacancy or hole in that shell, the vacancy will be filled by an electron from higher energy levels. Electrons can cascade from higher to lower energy levels and emit the characteristic photons or Auger electrons, with only few keV.

2.1.2 Coherent or Rayleigh scattering

When an incident photon interact with matter, coherent scattering may occur. In a classical physics description, the photon will interact will all electrons of the atom as a group, and not individually, and the energy lost in the process is neglected when compared with the initial energy of the photon. Therefore the scattered photon has approximately the same energy than the incident photon, and it also conserves its phase[13].

2.1.3 Incoherent or Compton scattering

For energies typically between 30 keV-30 MeV (depending on the photon energy), X and γ rays will interact mostly by incoherent scattering, also called Compton scattering, first described by H.G. Compton in 1923[14]. When an incoming photon interacts with shell electrons, it can transfer part of its energy to a single electron. This transferred

energy is much higher than the binding energy of that electron, so the electron is assumed to be at rest. This interaction is represented in Fig. 2.2. The electron will

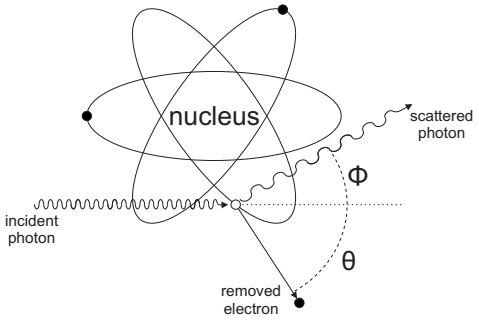

Figure 2.2: Classic schematic representation of Compton scattering. The photon is scattered with an angle of ϕ, while the electron recoil with an angle of θ in respect with the incident photon direction.

acquire kinetic energy and will be ejected with an angle θ relative to the direction of the incident photon. The photon will loose part of the energy and will be scattered with an angle ϕ. The energy of the scattered photon E_f can be calculated as 2.2

$$E_f = \frac{E_0}{1 + \frac{E_0}{m_e c^2}(1 - \cos\theta)} \tag{2.2}$$

where E_0 is the energy of the incident photon, ϕ is the scattering angle, m_e is the mass of the electron and c is the speed of light in vacuum. For lower-energy photons, almost all the energy after the Compton interaction will remain with the scattered photon, but for higher-energy photons, a very considerable amount of energy will is transferred to the recoil electron[13].

Doppler broadening

The relationship between the energy of the photons and the scattering angle assumes that the initial energy of the electron is zero, which is not true for shell electrons, since they have an energy that depends on the material and its physical state. This effect results in an angular uncertainty of the scattered photon[13].

2.1.4 Pair production

When an incoming photon with, at least, twice the rest energy of an electron is near a nucleus, an electron-positron pair can be created. The rest energy of each one of these particles is 0.51 MeV. The excess energy is released as kinetic energy of the pair particles.

Due to the positive charge, the positron is rapidly trapped in the medium and combines with some of the shell electrons in surrounding atoms, originating two identical annihilation photons, emitted in opposite direction, to keep momentum and energy conservation[13].

2.2 Transport properties of charged particles in gas media

Transport properties of charged particles (usually electrons or ions) in gas media are of the highest importance to understand gaseous detectors. Two approaches, macroscopic and microscopic, are used to describe the process of the drift of charged particles in gas media. A deep description can be found in Ref.[15]. From now on, we will assume drifts under the influence of an electric field and the absence of a magnetic field.

2.2.1 Macroscopic approach

The drift of charged particles in gas media is conditioned by the collisions with the particles of the gas. The nature of the collisions can be elastic or inelastic. Elastic collisions will only change the drift direction of the particle, so they are not very important for the generality of the applications. On the other hand, inelastic collisions transfer part of the energy of the particle to the gas atoms and are of great importance in the operation of gaseous detectors.

The drift of charged particles in a gas under the influence of the electric field can be represented by the following differential equation 2.3

$$m\frac{d\vec{v}}{dt} = e\vec{E} - K\vec{v} \tag{2.3}$$

where m is the mass and e is the electric charge of the particle, $\vec{v}$ is the velocity, $\vec{E}$ is the electric field and K is a friction term that includes all the microscopic collisions between the drifting particle and the particles of the gas, explained in subsection 2.2.2.

We can define the ratio $\tau = m/K$ as a characteristic time. For a time $t >> \tau$, equation 2.3 as a steady state solution, in which the acceleration $d\vec{v}/dt$ is null, the particle reaches a steady velocity, and we can write

$$\vec{v} = \frac{e\tau}{m}\vec{E} = \mu\vec{E} \tag{2.4}$$

The constant $\mu = \dfrac{e\tau}{m}$ is the ratio between the velocity of the particle and the electric field, in the absence of magnetic field, and it is called scalar mobility.

This formulation is made for macroscopic drift. We assume that all the possible microscopic interactions between drifting particles and gas particles are indistinguishable, being included in the friction term, and for larger drift time t, in average, the velocity of the drift particle will have the same direction than the electric field.

This approach remains valid if we are only interested in the drift properties like the mean velocity, drift direction or diffusion of a single particle. But once we want to include interactions like ionizations or excitations, microscopic approach is more suitable.

2.2.2 Microscopic approach

Since we are also interested in microscopic interactions between drifting particles and gas particles, we should concern about how drifting particles are scattered by the gas particles.

Considering an electron between two consecutive collisions, we can assume that the electron travels in vacuum, and during the path to the next collision, it will only be influenced by the electric field. After the first collision, due to its light mass, the electron will scatter in an isotropic manner, having no preferential direction after the collision. Let us considerer that the electron has an instantaneous and randomly oriented velocity v, due to the previous movement of the electron. Some short time τ after the first collision, the electron will gain extra velocity v_E, from the electric field

$$v_E = \frac{e\tau}{m}E \tag{2.5}$$

where E is the average intensity of the electric field between collision. This velocity corresponds to the macroscopic drift velocity, and τ represents the mean time between collisions, and justify the interpretation of τ as the ratio between the mass and the friction coefficient, given in subsection 2.2.1.

For an electron with total velocity v, the mean time τ between collisions can be expressed as

$$\frac{1}{\tau} = N\sigma v \tag{2.6}$$

where N is the density number of the gas and σ is the cross section of the gas (related with to collision probabilities).

In the next collision, the extra acquired energy will be lost through recoil, excitation or ionization with the gas particles.

The square of extra velocity v_E can be written as

$$v_E^2 = \frac{eE}{mN\sigma}\sqrt{\frac{\lambda}{2}} \tag{2.7}$$

where λ is the average fractional energy loss between two collisions (it is a dimensionless value). We know that λ is dependent of the energy of the electron. If the energy is below the excitation threshold of the gas, the scattering is manly elastic, and $\lambda \approx 10^{-4}$. The fraction λ is strongly dependent of the gas composition, and even slight changes in the gas composition can change in large scale the drift velocity of electrons due to different losses of energy during scattering.

In order to compare the drift velocity between different mixtures of gases, we need to adjust the ratio E/N, called reduced field. The usual dimensions of reduced fields are V cm^2.

At standard temperature and pressure (where the majority of the gaseous detectors work), E can be of the order of $10^2 - 10^6$ V cm^{-1} and N is of the order of 10^{19} particles cm^{-3}, and it is common to represent the quantity as E/p instead of E/N, where p is the pressure. It is expressed in V cm^{-1} Torr^{-}1. The conversion between the two quantities was suggested by L.G.H. Huxley et al. [16], when he introduced a new unity

for E/N the Townsend (1 Td= 10^{-17}V cm^2). The conversion between E/N and E/p, at a given temperature T, can be done using

$$\frac{E}{N}(\text{Td}) = (1.0354 \times 10^{-2} \times T) \left(\frac{E}{p}\right)_T (\text{V cm}^{-1} \text{ Torr}^{-1}). \tag{2.8}$$

2.2.3 Collisions during drift of charged particles

During the drift of the particles in the gas, different types of collisions can happen. In a general way, the collisions can be elastic or inelastic, and for inelastic collisions, a general distinction between excitations and ionizations is made. Let us consider again the drift of an electron under the influence of an electric field.

Elastic Scattering

This collisions occur preferentially for smaller values of electron energy. In elastic collisions, the conservation of kinetic energy and momentum of the system remains valid. The electron collide with gas particles, and can change its energy and the direction of the movement. Only the drifting electron and the gas particle participate in the collision.

Inelastic Scattering: Excitations

Inelastic collisions can occur when the kinetic energy of the system is not conserved. For sufficiently high drift energies, above the so-called excitation threshold (value of the electric field above which the electron gains enough energy to excite the gas atoms or molecules during collisions), the electrons can collide with gas particles, transferring part of the energy to the electronic cloud of the particle. Some electrons in the shells can acquire energy to go to excited states, decaying after to the ground state, with emission of a photon and/or collisions with other particles of the gas. This is the method used for light amplification in gaseous detectors.

Inelastic Scattering: Ionizations

If the drift electron has energies above the ionization threshold, defined as the electric field value above which the electron gain sufficient energy to ionize gas particles during the collisions, ionization may occur. A shell electron is ejected from the electronic cloud and released to the gas. This is the principle of the charge amplification in gaseous detectors.

For sufficiently higher electric fields, ionizations are frequent and each primary drifting electron can produce an avalanche of secondary electrons. After ionizations, positive ions and ejected electrons will drift in opposite directions, due to the presence of the drift electric field, and will no longer recombine.

2.2.4 Diffusion

During the drift in the gas, charged particles will suffer several elastic collisions, which can change the drift direction. For ions, collisions do not play an important rule

in the drift, due to its high mass, so they follow very well the field lines of the applied electric field.

This is not valid for electrons, because they are lighter. Although electrons will in general follow the direction of the electric field (defined as longitudinal direction), transversal diffusion will occur, and it depends in the intensity of the electric field, the temperature and the longitudinal travelled length.

Considering a longitudinal electric field, parallel with the zz's axis, transversal diffusion follows a Gaussian distribution, with standard deviation, for the projection in xx' axis, is given by 2.9

$$\sigma_x = \sqrt{2Dt} \tag{2.9}$$

where D is the transverse diffusion coefficient, and t is the time elapsed since the electron start the drift.

We can rewrite the last equation as

$$\sigma_x = \sqrt{\frac{2kTL}{eE}} \tag{2.10}$$

where T is the temperature, E is the magnitude of the electric field and L is the longitudinal path.

With this relation, we can predict that intrinsic transversal diffusion will increase with temperature and longitudinal path, and decrease with higher electric fields, and most of all, it does not depend in the nature of the gas. This diffusion is an intrinsic phenomena from Brownian movement, and σ_x is named *thermal limit*. Its value is the minimum achievable diffusion value.

For a deep description, the reader is invited to read section 2.2.4 in[15].

2.2.5 Penning properties

The drift of accelerated electrons above the excitation threshold, in pure noble gases, may excite an electron from the atom through a collision. The mechanism to release the excess of energy is a radiative decay. If a quencher molecule (like CO_2) is introduced in the gas, this opens a new way for the noble gas de-excitation: the excess of energy can be transferred from the noble gas to a quencher molecule. If this energy is above the ionization threshold of the quencher, an ionization may occur, with a probability called Penning probability. This is known as the Penning effect. [17, 18].

2.3 Radiation detectors principles

Once an incoming particle interacts with the gas of a gaseous detector, there are several ways to detect the interaction. The main difference between the different operation principles of gaseous detectors is related to intensity of the electric potential used by the detector. In Fig.2.3 different operation regions of gaseous detectors are shown.

When the potential is lower, the incoming particle ionize the particles of the gas, originating the primary cloud. The weak potential is not sufficient to avoid all the

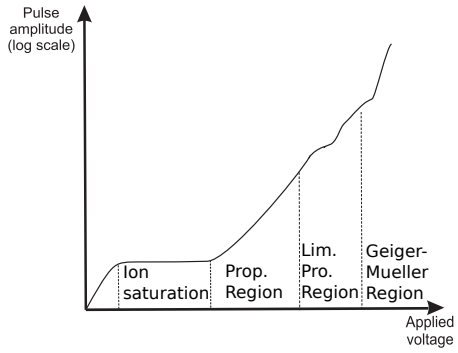

Figure 2.3: Pulse amplitude of the detected signal of an incoming particle, as a function of the potential applied to the gaseous detector. We can distinguish four different operation regions [5].

---

recombinations between primary electrons and ions. Due to this fact, only few electrons will be collected and the tracked signal will be lower than the original one.

Increasing the potential, but still under the ionization threshold, recombinations will be suppressed. For this range of potentials, primary electrons will not ionize new particles of the gas, but the collected charge reflect the properties of the interactions in terms of deposited energy. This operation region is known as the ion saturation region.

If an increase in the potential is made, the potential will overcome the ionization threshold and primary electrons will gain sufficient energy to originate a Townsend avalanche. Since each electron will be accelerated by the electric field with the same intensity, the number of secondary electrons in each avalanche will be, in average, the same. Therefore, the final number of collected electrons will be proportional to the number of primary electrons, which in turn are proportional to the energy deposited by the interacting particle. This is known as the proportional region operation of gaseous detectors. The detectors studied in this work can operate in proportional and ion saturation region.

For higher potentials, non-linearities in the detector response will appear. If the potential is higher, the magnitude of the avalanches will also be higher (more ionizations per avalanche), and each ionization will occur closer to the others, originating positive clusters of ions in the first instants of the avalanche, since ions are slowly evacuated than electrons. This positive clusters will slightly change the local electric field, changing the number of secondary electrons in each avalanche, that is no longer equal for all the avalanches. We are now in the region of limited proportionality.

If the potential is increased even more, then the local field created by the cluster of charges in each avalanche will be dominant over the field created in the detector. Avalanches will occur until all the charges are collected, and there is no further proportionality between the energy deposited by the incoming particle and the number of secondary charges in the avalanche. The signal amplitude now gives only information of the number of interacting particles in the gas, and no longer information of the energy of that particles. This is called the Geiger-Mueller region.

2.4 Charge amplification in gaseous detectors

The charge amplification is a type of signal amplification used very often in gaseous detectors. This operation mode is also known as *Townsend avalanche* stage.

A drifting electron, accelerated by an electric field above the ionization threshold, can produce additional secondary electrons as consequence of collisions with gas particles. The avalanche produced by this process is called the *Townsend avalanche*.

The increase in the number of produced electrons n, per unity of path distance x, is represented by the Townsend equation:

$$\frac{dn}{n} = \alpha(E(x))dx \tag{2.11}$$

where α is the *first Townsend coefficient* of the gas, and is dependent of the intensity of the electric field, being zero for values bellow the ionization threshold of the gas. The gain or *gas multiplication factor*, $M = n(x)/N_e$, is the average number of produced electrons at a given value of x, for N_e initial electrons, can be calculated by the integral over the path Γ:

$$\ln M = \int_{\Gamma} \alpha(l)dl \tag{2.12}$$

where $\alpha(l)$ is the Townsend coefficient at a given position. If the electric field is constant over the path, then the equation can be simplified to $M = e^{\alpha x}$, and the gain increases exponential with the drift distance x.

2.4.1 Proportional counters

Proportional counters are devices operating in the proportional regime and widely used for X-ray detection since they show good energy resolution[19]. They consist in a gas chamber and two electrode, with a tube (cathode) connected to the ground, and with a thin wire (anode) at a given potential V, as shown in Fig. 2.4a.

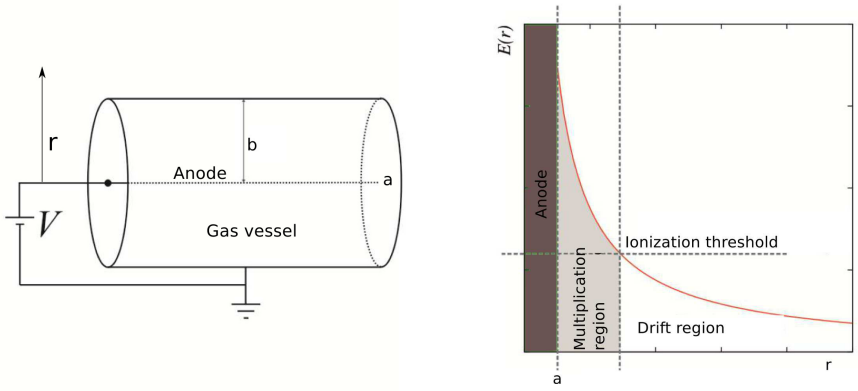

(a) (b)

Figure 2.4: a) Tube proportional counter. b) Representation of the intensity of the electric field inside the proportional counter, as a function of the distance r to the center of the anode[5].

The intensity of the electric field for this proportional counter can be written as

$$|\vec{E}| = \frac{V}{r \ln \frac{b}{a}} \tag{2.13}$$

where V is the voltage between electrodes, r is the distance to the center of the anode, with radius a, and b is the cathode's radius. As we can see in Fig.2.4b, bellow a given value or r, the electric field is above the ionization threshold of the gas, primary drifting electrons can ionize gas particles and create an avalanche. Avalanche electrons are collected in the anode, and the detected signal is proportional to the number of primary electrons.

2.4.2 Micro Pattern Gaseous Detectors

Micro Pattern Gaseous Detectors (MPGDs) were developed to detect radiation, and the main applications are for high energy physics, astrophysics, dark matter research and medical imaging[19, 20, 21, 22]. These devices have dimensions of the order of the micrometers, where the nodes and cathodes, placed in an insulator support, are separated by a few tens of microns, allowing to reach very high electric fields at low voltages.

Conductive layers can be etched in different ways to produce different patterns and geometric configurations, and the different sizes of the layers and the etched pattern will make the distinction between MPGDs.

These devices work inside a gas, usually noble gases or mixtures containing them. Due to the geometric configuration of the MPGDs, when a potential is applied between the two electrodes, an intense electric field inside and in the edges of the holes of the insulator is created. This electric field can be higher than the excitation and/or ionization threshold of the gas, meaning that an incoming electron accelerated by the electric field can excite and/or ionize other particles of the gas.

There are several MPGDs that are used nowadays. In this work we will focus our study in two of the most widely used the *Gas Electron Multipler* (GEM) and the *Thick-Gas Electron Multipler* (THGEM).

Gas electron multiplier - GEM

The GEMs detectors are one of the simplest MPGDs. They were first suggested by Fabio Sauli in 1996[9]. They consists of a general thin polymer foil metal-clad in both sides, and with a large density of etched holes through the polymer and metal foils. These etched holes are usually bi conical holes in the polymer foil, but cylindrical holes are also used in some particular GEMs[23]. The holes are distributed in an hexagonal pattern. In the case of general made GEMs, the dimensions are 140 μm between consecutive holes, the polymer thickness is 50 μm and metal electrodes are 5 μm thick. The external diameter of the hole is 70 μm and the internal is 50 μm. In Fig. 2.5a a schematic cross-section of the considered GEM geometry and a scanning electron microscopy image of a real GEM device is shown in Fig. 2.5b.

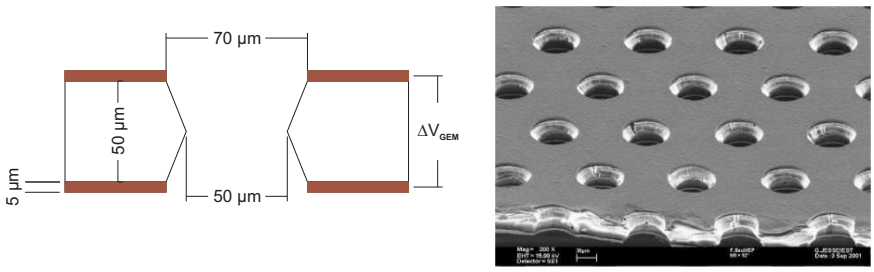

(a) (b)

Figure 2.5: a) Cross section a GEM, with typical dimensions and the voltage applied between electrodes. b) Close view of a real GEM foil, where we can see the hexagonal distribution of the holes, image taken from [24].

Thick-Gas electron multiplier - THGEM

The Thick-GEM, or simply THGEM, is a GEM-like device. It consist of a polymer thin layer metal-clad in both sides, with an hexagonal distribution of the holes. On the case of the THGEMs, the dimensions are usually larger than the GEMs dimensions. The distance between holes is normally 0.7 to 4 mm, the thickness of the polymer foil is usually 0.4 to 3 mm, the holes are cylindrical, with diameters from 0.3 to 2 mm, and it is also usually to etch a rim in metal layers with up to 0.2 mm distance around the holes [10]. The main geometric differences between GEMs and THGEMs are the size, the presence of etched rim in THGEMs. The rim is used to decrease the discharge probabilities, allowing higher potentials and gains with low discharge probability. A THGEM cross section is represented in Fig. 2.6a and a real image taken with optical microscope is shown in Fig. 2.6b.

The THGEMs studied in this work have an hexagonal hole pattern, in which the distance between holes is 0.8 mm, the insulator thickness is 0.4 mm, the metal layer are 0.029 mm thick, the hole diameter is 0.4 mm and the rim width dimensions varies from 0 (no rim) to 0.15 mm.

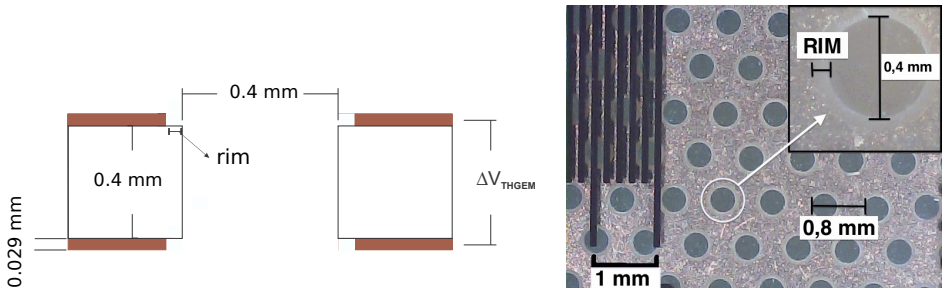

(a) (b)

Figure 2.6: a) Cross section a THGEM, with typical dimensions and the voltage applied between electrodes. b) Close view of a real THGEM foil, observed with optical microscope, where we can see the hexagonal distribution of the holes.

Chapter 3

Electroluminescence in noble gases

Electroluminescence, also known as secondary scintillation, is a process of luminescence where the emission of light is not followed by heat release. For more details of the topics covered in this chapter, see[5, 25, 26].

From the interaction of an incoming ionizing particle with the atoms or molecules of the gas in the detector, part of the energy of the ionizing particle will be transferred to gas particles. The particles of the gas can be excited or ionized due to this energy transfer.

From excitations, the particles of the gas can de-excitate to the ground state by light emission (the energy of the photons will depend on the energetic levels involved in the process). This light is called primary scintillation.

From ionizations, the cloud of produced primary electrons will drift by the electric field applied in the gas region. The energy acquired by primary electrons will depend manly in two factors, the intensity of the electric field $E = \|\vec{E}\|$ that is accelerating the electron between collisions, and the density of particles in the gas region, designed N. For electric fields above the excitation threshold, light emission can occur as a result of excitations. The light produced during the drift of electrons in the gas is called secondary scintillation or electroluminescence.

The *electroluminescence yield*, Y, is defined as the number of photons produced per primary electron, per unit of path length. This quantity is of the great importance since higher yields allow detection of weaker signs.

Since the energy of the electrons will depend in E and N, and N is dependent of the pressure and temperature, it is common to express the reduced yield Y/N as a function of reduced electric field E/N. This relation therefore is not influenced by temperature and pressure.

3.1 Microscopic description

The emission spectra of noble gases is a consequence of the various deexcitations and recombination processes. The excitation levels responsible for the light emission come from atomic levels (optical, resonance or metastable levels) or molecular levels, being some impurity levels responsible for emission suppression.

The fundamental electronic atomic level in noble gases is located in np^6 orbitals (except for Helium that has the lowest occupied orbital is ns^2), where n is the first

quantum number. These orbitals are completely filled with electrons in the ground state. Excited states are created when an electron from the ground state will occupy a more energetic orbital ($n's$,$n'p$,$n'd$,etc), by energy absorption, Once an electron goes to an excited state, it will return to the ground state by releasing the excess energy. The atomic levels produces strait lines in the atomic spectra. At pressure above few tens of mbar, the three are unlikely to occur, in comparison with the molecular processes.

For pressures above few tens of bars, molecular emission is predominant. It produce a continuum distribution centered at VUV wavelengths, but the presence of some impurities can suppress radiation emission or shift the wavelength. We will focus our attention in molecular emission at VUV range since it is the most widely used in gaseous detectors at a standard pressure.

3.2 VUV molecular emission

Molecular excited states can originate VUV emission. The collision of a generic excited atom, R^*, with two atoms in the ground state, R, will form an *excimer*, electronically and vibrationally excited molecules, R_2^{**}:

$$R^* + 2R \longrightarrow R_2^{**} + R \tag{3.1}$$

Two different ways of returning to ground state may occur. On one hand, the excimer R_2^{**} can decay directly to ground state, resulting in two separated atoms, R, and the emission of one photon hν_1:

$$R_2^{**} \longrightarrow 2R + h\nu_1 \tag{3.2}$$

On the other hand, the excimer can first collide with one neutral atom, and lose vibrational energy during the collision:

$$R_2^{**} + R \longrightarrow R_2^{*} + R \tag{3.3}$$

and finally the resulting excimer in the lower vibrational energy will emit a photon hν_2, and be separate into two neutral atoms:

$$R_2^{*} \longrightarrow 2R + h\nu_2 \tag{3.4}$$

The photons produced in 3.2 will produce the so-called *first continuum* emission, and the emitted radiation described in 3.4 will produce the *second continuum*. Above few hundred of mbar, the process resulting in the emission of the second continuum is favored, due to a large number of collisions, and the second continuum is predominant. The peak positions of the second continuum for gaseous xenon, argon and neon are 170.9 nm, 126.5 nm and 80 nm, respectively[26, 27, 28, 29, 30, 31].

The decay from excited molecular states can also originate photons in VIS-IR (Visible to Infra-red) range, depending in the energy of the excited state[32]. Electroluminescence yield of VUV and VIS-IR photons are defined as Y_{VUV} and Y_{VIS-IR}.

For lower values of E/N, accelerated electrons do not have enough energy to excite particles of the gas, so both Y_{VUV} and Y_{VIS-IR} will be zero. If E/N is increased above the VUV excitation threshold, then VUV photons will start to be emitted during

excitations, resulting from the decay of the first excited states of the excimers.

If $\frac{E}{N}$ is increased even more, more excited states will be available, and a ground electron can occupy high energy levels. The decay process will normally occur in two stages: first the electron decays from the excited orbital to a lower energy orbital (not yet the ground state), emitting a VIS-IR photon, and then it decays to the ground state, with an emission of a VUV photon. Therefore, the emission of a VIS-IR photon is followed by a VUV photon emission, so $Y_{VUV} > Y_{VIS-IR}$. For a higher value of E/N ionizations start to happen.

The importance of the gas purity in electroluminescence production is related with the number of elastic collisions that the electrons needs to acquire enough energy to excited the molecules. If molecular impurities exists, there is a significant probability for the electron to lose part of the energy in rotational and/or vibrational states of the impurity. If this happens, the electron will not gain enough energy to produce electroluminescence, and the light emission is suppressed, reducing electroluminescence yield[33]

Chapter 4

Simulation toolkit

The response of the MPGD in terms of particle detection and effective gain have been simulated using three programs.

For simple configurations (i.e. drift in constant electric fields), Garfield++[34, 35] can be used to simulate the drift and transport properties of charged particles inside a gas. Garfield++ has an interface with Magboltz [36, 37], a program based in Monte Carlo methods that simulate collisions of particles for nearly arbitrary gas mixture.

Only the previous two programs are needed when simple configurations are considered, but due to the existence of an insulator-gas interface in the MPGDs, an analytic solution for the electric field in the region of interest is not possible to obtain because of the discontinuity in the electric permittivity in the interfaces, and Garfield does not numerically solve Maxwell equations. To overcome this issue, the electric field needs to be computed with external software that gives numerical solutions. Some software is available and the most commonly used are based in *Finite Element Methods* (FEM) approach. In this study we used Ansys[1].

The electric field is calculated along discrete nodes in a mesh, using boundary conditions, and interpolate the electric field values to the remain space, saving the data to field map files. Using these three programs, we can simulate nearly arbitrary detector and gas mixture. Each software is briefly described below.

4.1 Garfield

Garfield was developed by Rob Veenhof at CERN. Originally written in Fortran, has recently migrated for a C++ version, named Garfield++, which has a useful interface with ROOT[38], a data analysis software developed at CERN. It was first developed to simulate gaseous detectors, such as drift chambers, where the electric field has analytic solutions.

For those calculations, the program only requires the electric field configuration in the MPGD. It can calculate the field maps for some particular geometries, but for more general geometries, it has an interface to read FEM field maps. The Fortran version of Garfield implement Runge-Kutta-Fehlberg methods to determine the field lines of the electric field. These will be the drift lines followed by charged particles in

[1] www.ansys.com

vacuum. In gases, it uses the same approach to drift ions. Since ions are heavy, they tend to follow the field lines of the electric field without scattering. But electrons are lighter, their trajectory changes abruptly due to collisions with particles of the gas, and they don't exactly follow the field lines. An interface with Magboltz allow Garfield to use a Monte-Carlo based method to drift electrons, instead of Runge-Kutta-Fehlberg methods.

On the C++ version of Garfield has not yet been implemented Runge-Kutta-Fehlberg methods. Instead, it always uses of the interface of Magboltz to apply Monte-Carlo methods.

4.1.1 Runge-Kutta-Fehlberg methods

For electric field configurations constant in time, used in this study, the trajectory $\vec{r}(t)$ of a charged particle with mass m and charge e, under an electric field $\vec{E}(x, y, z)$, in vacuum, follow the differential equation:

$$m\frac{d^2\vec{r}(t)}{dt^2} = e\vec{E}\left(\vec{r}(t)\right) \tag{4.1}$$

To solve 4.1, Garfield uses Runge-Kutta-Fehlberg methods to calculate numeric solutions by this way, calculate the drift of the particle. Numerical solutions obtained works well for particles in vacuum, but if we have a gas, the collisions between the drift particle and the gas may affect the drift.

When we simulate the drift of ions or heavy particles, we can use the implemented Runge-Kutta-Fehlberg methods in Garfield, but to calculate the drift of electrons, we should use other methods that take the collisions into consideration.

4.2 Magboltz and Monte-Carlo techniques

Magboltz was developed by S. Biagi for solving the Boltzmann transport equations for electrons in gas mixtures when electric and/or magnetic fields are applied. It is based in Monte-Carlo methods, and uses cross sections calculations for various collision probabilities and different gas mixtures, calculating the probability of occurring each collision type (elastic, ionization or excitation).

If an electron starts the drift at $\vec{r}_0 = (x_0, y_0, z_0)$ with velocity $\vec{v}_0 = (v_{x_0}, v_{y_0}, v_{z_0})$, under the influence of an electric field $\vec{E}(x, y, z)$, that it is assumed to be constant between collisions, i.e. $\vec{E} = (E_x, E_y, E_z)$ for drift between $\vec{r}_0$ and $\vec{r}_1$ and for smaller time steps Δt, the position $\vec{r}_1 = (x_1, y_1, z_1)$ and velocity $\vec{v}_1 = (v_{x_1}, v_{y_1}, v_{z_1})$ after a time Δt between collisions, are given by the equations 4.2.

$$\vec{r}_1 = \begin{cases} x_1 = x_0 + v_{0_x}\Delta t + \frac{1}{2}\frac{e}{m}E_x\Delta t^2 \\ y_1 = y_0 + v_{0_y}\Delta t + \frac{1}{2}\frac{e}{m}E_y\Delta t^2 \\ z_1 = z_0 + v_{0_z}\Delta t + \frac{1}{2}\frac{e}{m}E_z\Delta t^2 \end{cases}, \vec{v}_1 = \begin{cases} v_{x_1} = v_{x_0} + \frac{e}{m}E_x\Delta t \\ v_{y_1} = v_{y_0} + \frac{e}{m}E_y\Delta t \\ v_{z_1} = v_{z_0} + \frac{e}{m}E_z\Delta t \end{cases} \tag{4.2}$$

where e and m are the charge and the mass of the drifting particle, respectively, and the values of the electric field E_x,E_y,E_z are loaded from the map fields.

After each collision, the position $\vec{r}$ and velocity $\vec{v}$ are updated according to the collision type that the particle suffers. Between collisions, it is assumed that the particle drifts in vacuum. The probability of the particle drifting during a time Δt between collisions follows an exponential distribution, which is given by the equation 4.3:

$$P(\Delta t) = exp(-\frac{\Delta t}{\tau}) \tag{4.3}$$

where τ is the *mean free time* between consecutive collisions, which is calculated in equation 4.4, at a given atomic density of the gas, N, velocity before the collision, v, and total cross section for drifting particle, σ:

$$\tau = \frac{1}{Nv\sigma} \tag{4.4}$$

where $\sigma = \sum_i \sigma_i$ is the sum of all individual cross sections for each possible collision. The cross sections used in this study are part of the LXcat project [39], an open-source website that collects cross sections of electron scattering for a large variety of gas mixtures. An example of the cross section for electron scattering of Xenon is shown in Fig. 4.1.

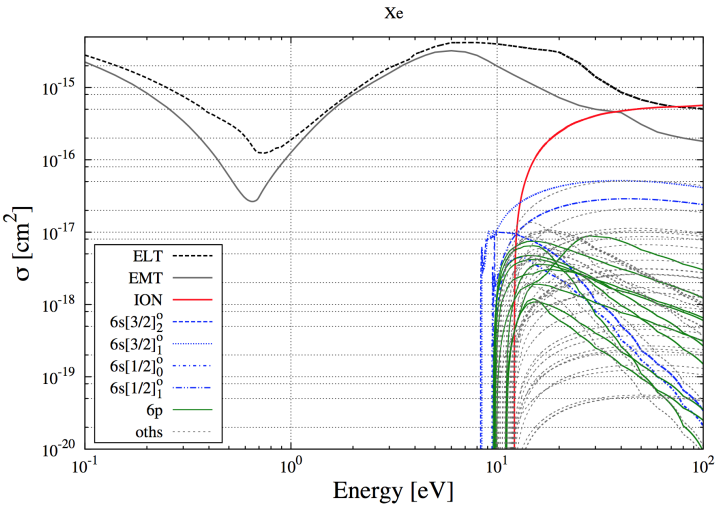

Figure 4.1: Xenon cross section for various collision[39].

4.3 Ansys

The application of electric potential to the electrodes of the MPGD can be treated as a boundary condition electrostatic problem. Therefore, FEM can be used to numerically solve this boundary problem and give solutions to Maxwell equations in the region of interests of the MPGD (drift medium and edge surfaces).

4.3.1 Finite element methods in Ansys

First, Ansys will discriminate the volume of interests (or areas, for 2D problems) in small sub volume elements, called finite elements, using a smart mesh to fill all the space. Each element is connected to its neighbours by nodes, being each node characterized by its position $\vec{r} = (x, y, z)$ and by the electric potential $\Phi(x, y, z)$. The position $\vec{r}$ is known for all the nodes in all finite elements. For the boundary nodes (located in the surfaces in which electric field is defined as initial condition, like electrodes) we know the exact value of the electric potential. For the remaining nodes and space, the potential is interpolated by polynomial functions.

4.3.2 Choosing finite elements

Depending on the problem, Ansys allow choose between different types of finite elements to best fit each situation. In this particular 3D electrostatic situation, we chose tetrahedral elements with curved edges and 10 nodes, manly because they can easily fit the sharper geometries in the MPGDs, like the holes in GEMs. An example of a tetrahedral element can be found in Fig.4.2a. Ansys can automatically adjust the number and the size of the elements in particular regions of interest, where we require more accuracy in the calculations or simply where electric potential change more drastically. An example of a mesh in a GEM with elements of different sizes is also shown in Fig. 4.2b.

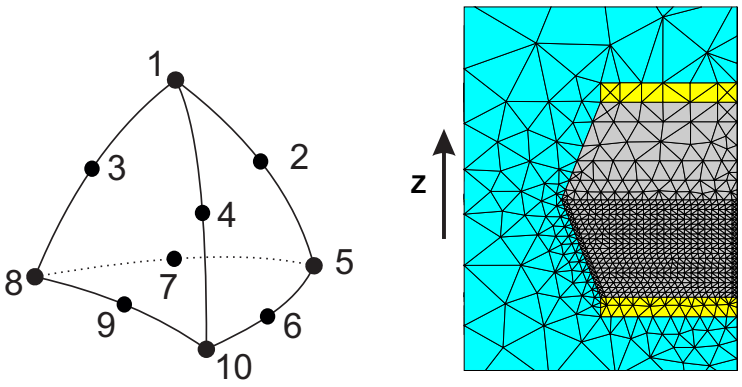

Figure 4.2: a) Representation of the tetrahedral electrostatic finite element used in Ansys for electrostatic calculations. b) Example of the volume of the GEM meshed with finite elements.

4.3.3 Interpolation functions

Once the electric potential is calculated in all the nodes of the mesh, Ansys will compute the potential in all the remaining space. Interpolation functions are used for these calculations, usually polynomials, since they are easily differentiated and integrated. The main problem with polynomials is that they are not solution of the Maxwell equations, therefore introducing errors in the calculations.

There is another software that is under development for this kind of electrostatic calculations, based in Nearly Exact Boundary Element Methods, the so-called neBEM[40]. It consists of a new approach to solve these problems numerically, using Green functions instead of polynomials. Contrary to polynomials, Green functions are solutions of Maxwell equations. This software is expected to be integrated with Garfield++ in the near future.

Using polynomial interpolation, the electric potential inside a tetrahedral finite element with curved edges, is given by the eq. 4.5.

$$\Phi(x,y,z) = a_1 + a_2x + a_3y + a_4z + a_5x^2 + a_6y^2 + a_7z^2 + a_8xy + a_9xz + a_{10}yz \quad (4.5)$$

where (x,y,z) are the spacial coordinates of the point in which we want to calculate the electric potential and $a_{1..10}$ are coefficients calculated with the electric potential of each nodes.

The correspondent electric field, $\vec{E}$, can be calculated as the gradient of the electric potential $\vec{E} = -\vec{\nabla}\Phi$ [41]:

$$\vec{E} = (-a_2 - 2a_5x - a_8y - a_9z, -a_3 - 2a_6y - a_8x - a_{10}z, -a_4 - 2a_7z - a_9x - a_{10}y) \quad (4.6)$$

The FEM applied in Ansys force a continuity in the electric potential between shared nodes in neighbour finite elements. This is one of the strengths and, at the same time, one of the weaknesses of this method, because it is capable of guaranteeing the continuity of the electric potential, but not the continuity of its derivative, the electric field, that is not discontinuous along the same medium.

Another problem of the method is the calculation of the electric field in non-irradiated MPGDs. When we are not irradiating the MPGD, the density charge in the drift gas should be zero, and the Poisson equations is simply 4.7

$$\nabla \bullet \vec{E} = 0 \quad (4.7)$$

but if we apply the gradient operator to the expression 4.6, we will get eq. 4.8:

$$\nabla \bullet \vec{E} = -2a_5 - 2a_6 - 2a_7 \quad (4.8)$$

that is different from 0 for almost every general situation, since $-2a_5 - 2a_6 - 2a_7 = 0$ only for particular values of electric potentials in the nodes. This is a consequence of polynomials not being solutions of Maxwell equations.

Chapter 5

Gain simulations in GEM and THGEM

One of the first goals of this work is to study some properties and the operation modes of MPGDs, to be able to manipulate geometric and electromagnetic parameters in the simulations and extrapolate interesting results for real detectors.

The simulations were divided into two sections. First we studied the *charging-up effect*, which is likely to be responsible for instability of the gain over time and for the discrepancy between simulated and calculated results. Second we studied the influence of the variation of some THGEM geometric dimensions (the thickness and the rim) in the simulated gain.

5.1 Charging-up effect

The operation principle of the MPGDs is based in the drift and the collection of charges in the gas.

Though these charges, during their drift through gas, they tend to follow the electric field lines. Collisions with the gas particles make the path of the charges change, especially for electrons, and some of them can be trapped in the insulators surfaces of the detector5.1. Electronic affinity of the polyamide usually used as insulator in GEM fabrication is 1.4 eV[42] meaning that if an electron during the drift is trapped in the insulator, an energy of 1.4 eV is needed to remove it.

Ions trapped by the insulator will behave in another way. Once they touch the insulator surface, they trap an electron from the electronic cloud of the insulator molecules or a previously trapped electron, becoming neutral again. The new formed atom return to the gas and one positive charge is transferred to the insulator as holes[43].

The accumulation of these charges will change the local electric field in the insulator. The described phenomenon of charge accumulation in the insulator surfaces is known as the *Charging-up* of insulators. Once trapped, charges will still be able to move through the surface or the bulk of the material, in which the bulk mobility is more likely to occur[44]. Some authors refer that the time to evacuate these charges can be of the order of minutes to some hours[45]. For the propose of our simulations, we are assuming that the charges trapped in the insulator do not move any more during the remaining process. This is valid as long as the charging-up is faster than the

time needed to evacuate these charges, i.e., during the initial moments of the detector irradiation.

The size of the avalanches depends highly in the electric field inside and near the holes of the MPGDs, and since charging-up can change this local electric field, it has the potential to change the gain of the detector.

Studying this effect is of great importance in order to better understand the response of MPGDs in terms of charge and light amplification.

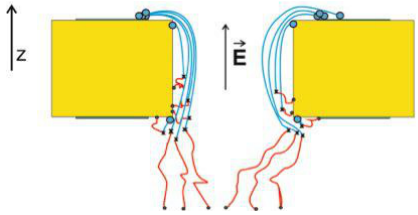

Figure 5.1: Charging-up illustration in a THGEM. Blue dots represents the ions, red dots represents the electrons, the marks are the ionization position and the lines are the drift path of the particles.

5.1.1 Motivation

The charge gain in MPGDs depends in various factors: pressure, temperature and gas purity, non-uniformity in the detector geometries, applied voltages, among others. Since the first attempts to study the fundamental behaviour of the charge gain in MPGDs with simulations, the charge gain is not fully understood and cannot be completely modelled. Common measurements with GEMs and THGEMs show that the gain of the detectors is usually is not stable during the initial minutes or hours of measurement, and differences between absolute gain value for simulations and experimental data were also observed. [46, 47, 48, 49] However, a Monte-Carlo method used for light gain simulations in uniform electric field was validated with experimental results, suggesting that the discrepancy in the simulation and measurement charge gain in MPGDs could be due to physical reasons. One of the causes could be the charging-up.

Initial simulations described in Fig. 5.3a and 5.3c show that in an ideal scenario (ideal geometries, pure gas, and so on), part of the secondary drifting charges would stop in the insulator surfaces, changing the electric field. Therefore, sufficient charge deposition may change the charge and light gain.

5.1.2 Gases

In order to compare our simulation with measurements available in literature, in the case of the GEM, the considered gas mixture was Argon 70 % / CO_2 30 %. The drift and induction fields were 0.2 and 0.3 $kVcm^{-1}$ respectively. Since this mixture is a penning-mixture, we considered the penning factor of 0.7. Recent studies shows that a more precise value for the penning probability of this gas mixture should be 0.56 [50][51].

Regarding the simulation with THGEM, a gas mixture of Neon 95% / CH_4 5% was considered, since it was our intention measuring charging-up in our lab and this

mixture was one of those that were available. The drift and induction electric fields were 0.2 and 0.5 kVcm^{-1} respectively. Although this is also a Penning mixture, we didn't find any reference for the correspondent penning factor, so we decided not to include it in the simulations. In principle, the exclusion of the penning probability will decrease the size of the avalanches for this mixture. Simulations were always performed considering room temperature of 293 K and a pressure of 760 Torr.

5.1.3 Initial attempts

Charging-up calculations are usually very time-consuming and last several days for computing useful information. To keep a great compromise between the charge gain of the detector, related to the time needed for charging-up effect, and the computational time for simulations, a potential of 400 V between electrodes was used for the first simulations in GEMs and 600 V in THGEMs. The simulation time depends manly in the number of simulated primary electrons, the size of the avalanches and the number of calculated collisions. Higher voltages in GEMs and THGEMs increases exponentially the size of the avalanches, resulting in more simulation time required. These potentials are not large enough to make extremely heavy simulations (very high gains), neither so small that long simulations would be needed to observe charging-up. Other potentials were studied later.

To start the study charging-up in GEMs and THGEMs we simulated the charge deposition in insulator surfaces in an uncharged situation.

In the case of the GEM, we randomly distributed 10^4 primary electrons in a unitary cell of the GEM at the initial z equal 100 μm above the GEM plane. For the THGEM, the same 10^4 primary electrons were distributed in the unitary cell area, and the start z was 1000 μm above the THGEM. These values of z correspond to the starting plane for primary electrons in Fig. 5.2a and 5.2b.

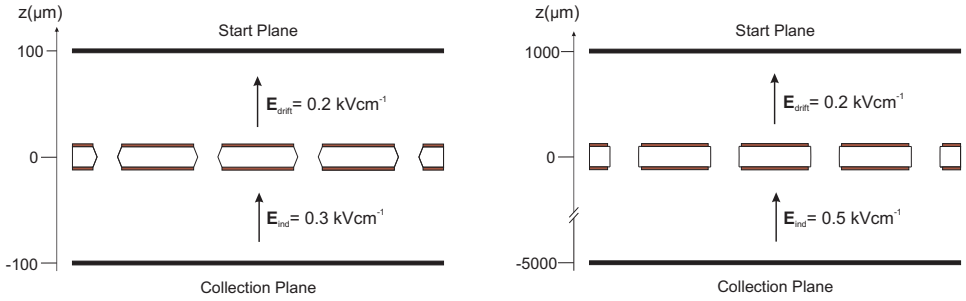

Figure 5.2: Cross section of the simulated configuration for a GEM(a) and THGEM (b).

In order to determine the number of collected and deposited electrons and ions, the final position of each electron and ion from avalanches is recorded:

- Electrons are collected if the final z is -100 μm bellow the GEM and -5000 μm bellow the THGEM (the collection planes are represented in figures 5.2a and 5.2b).

- Ions are collected if the final z coordinate is in the top electrode of the GEM or THGEM.
- Electrons and ions are deposited if after the drift the z coordinate is between the insulator coordinates (-25 μm to +25 μm in GEM and -200 μm to +200 μm in THGEM).

The deposition pattern of charges (electrons and ions separately) in the insulator, in the case of uncharged MPGDs, is shown in figures 5.3a and 5.3c, for GEMs and THGEMs respectively. We can see an irregular distribution of deposited charges in the insulator along the hole surface, in which a gradient potential will be created. After

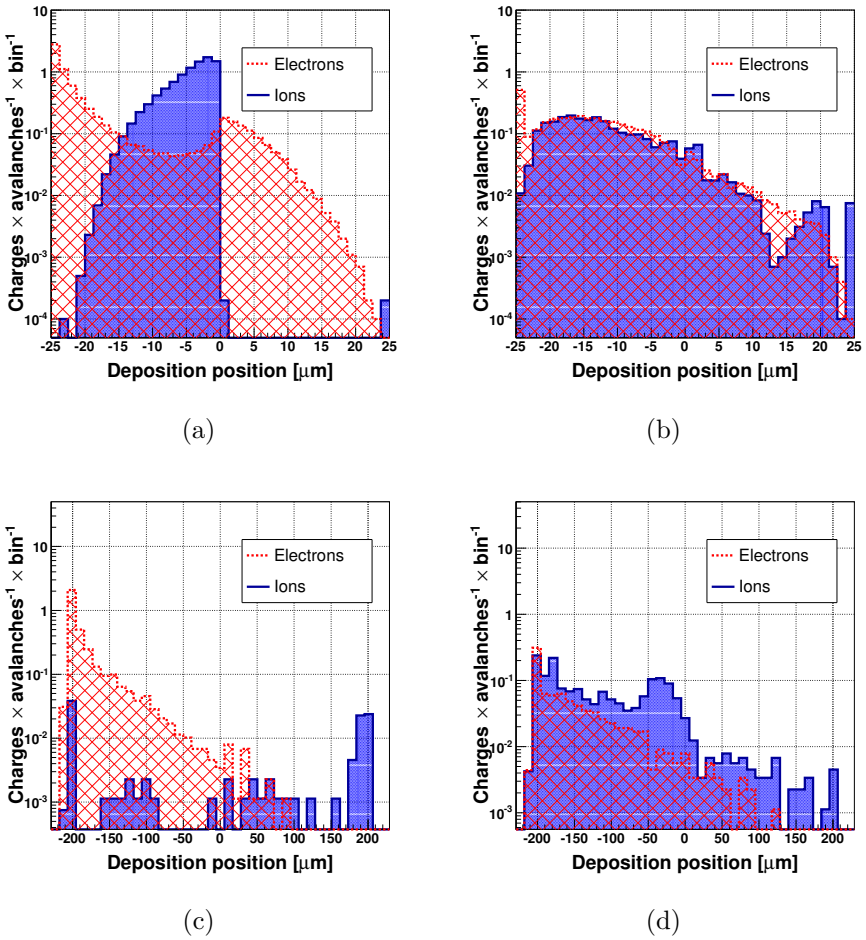

Figure 5.3: a) Uncharged GEM. b) Charged GEM. c) Uncharged THGEM. d) Charged THGEM. Histograms of the deposition of electrons(red) and ions(blue) in the insulator surface of a GEM and a THGEM, before and after charging-up, for 400V and 600V, respectively.

some avalanches, the distribution of the new electrons and ions that reach the insulator will tend to compensate each other, as shown in fig. 5.3b and 5.3d, due to the local field created by previously deposited charges. The variation of the local electric field will tend to disappear after deposition compensation.

We need to iteratively include this charge deposition in the fields maps. Ansys do not provide an option to put single charges in their particular deposition point in the

insulator surface. Instead, we need to create small slice surfaces in the insulator foil and iteratively add the correspondent density charge to each surface. Due to the shape of the deposition, and to computational limitations of field maps files for small finite elements, we use 24 different slice surfaces in the insulator, not regularly distributed, for GEM, as shown in figure 5.4a, and 20 equally distributed slices surfaces for THGEM, as shown in fig. 5.4b.

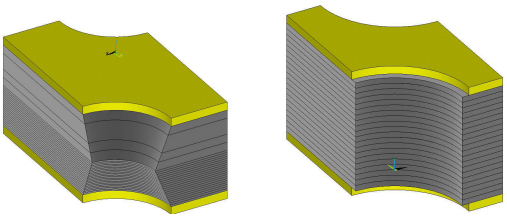

(a) GEM unity cell. (b) THGEM unity cell.

Figure 5.4: a) GEM unity cell. b) THGEM unity cell. Both computed with Ansys.

5.2 Simulation algorithms

A correct simulation of charging-up in MPGDs must consider an iterative method with small steps for each iteration, making this kind of calculations very time-consuming and arduous. Robust algorithms must be developed to complete the calculations in a reasonable time and using the less computational resources as possible.

Two algorithms are suggested in this work: the first one is more detailed, using an constant step for all the iterations, and the second one uses a more flexible and dynamic step. The description and comparison between both methods is made in the next sections.

5.2.1 Constant method

The first iterative algorithm used to simulate charging-up iterations is depicted in Fig. 5.5.

At the first iteration, we compute the electric field map with the insulator without previous deposited charges. We import the field map into Garfield++, and a simulation of 10^4 primary avalanches is performed to determine the total charge deposited in each insulator slice surface. A new field map is created, now considering the contribution of the charges deposited in the insulator, completing the iteration. The total charge to consider in each slice is determined by taking into account the contribution of both ions and electrons ending up in the insulator surface.

A new set of 10^4 primary avalanches is simulated through Garfield++ and the process is repeated until the average number of deposited charges per avalanche stabilizes. Statistical fluctuations depend in the number of simulated avalanches per step, but the number of deposited charges per avalanche seems to be less sensitive to fluctuations than the effective gain, so it seems appropriated to use the stabilization of deposited charges instead of gain stabilization.

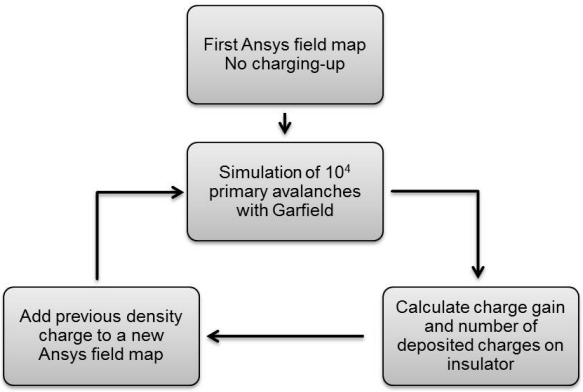

Figure 5.5: Constant step method diagram.

A small step of 10^4 primary electrons (corresponding, i.e, to $\sim$ 42 X-rays from a ^{55}Fe source with 5.9 keV) was chosen in order to obtain good detail in the evolution of charging-up over time. However, this small step implies hundreds of iterations until stabilization.

5.2.2 Dynamic method

In order to accelerate the simulation process, we developed an extension of this method that uses a dynamical step in each iteration. This step is smaller when the number of deposited charges per avalanche changes very quickly, and is larger when this quantity is more constant, i.e. the deposition stabilizes, which means that the effective gain also stabilizes.

To constrain the size of the step, a maximum size corresponding to the maximum charge that can be added to the new field map was defined as $2{\times}10^4$ new charges, the correspondent to 320 fC. This value ensures that the method does not use unreasonable step sizes. Our attempts show that this maximum step size is an acceptable value, but other limits can be used.

The dynamical method is briefly described in the diagram bellow.

The method starts with an uncharged Ansys field map of the MPGD. For each iteration we simulated 10^3 primary avalanches, in order to have good statistical values (10^3 primary avalanches is a good compromise between low statistical fluctuations and reduced computational time).

The number of deposited charges per avalanche, in each slice of the insulator surface, is multiplied by the variable step. For earlier iterations, steps between 0.5×10^3 and 10^3 primary avalanches were used.

After the first 5 iterations, we applied a first order fit to the deposition function of the previous iterations, and calculated, at a given step, what the value of that function should be for the new iteration.

We simulated iteration number 6, and compared with the predicted value of the function obtained with the fit:

- If the difference between simulated and fitted value was larger than the maximum defined step, we would discard the iteration, the step would be reduced to its half, and we would calculate a new iteration with the new step.

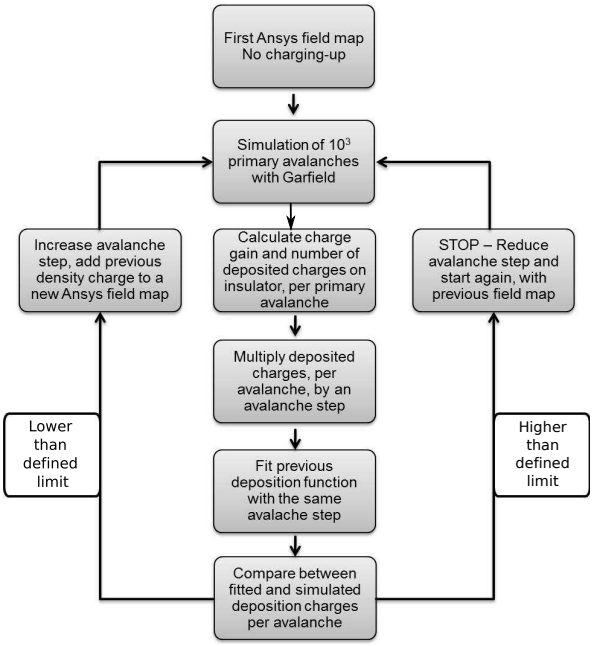

Figure 5.6: Dynamical step method diagram.

- If the difference between simulated and fitted value was smaller than the maximum defined step, the method would increase the step to the double, repeat the fit, including only the last 5 valid iterations

A visual example of the dynamic method is shown in Fig. 5.7b.

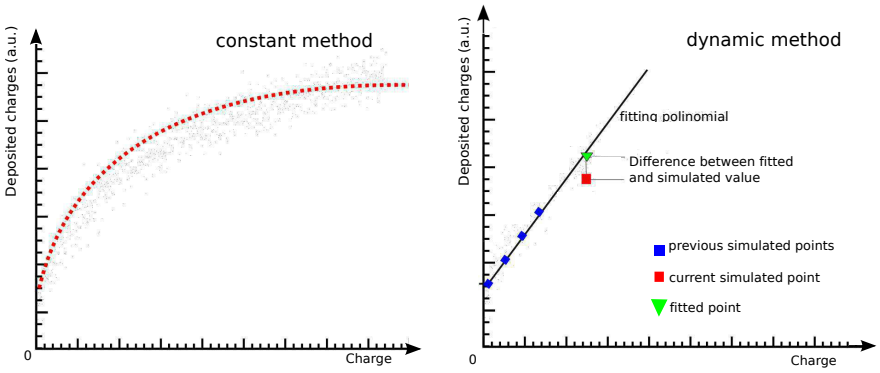

(a) (b)

Figure 5.7: a) Deposition function visualization for the constant method, each point represent an iteration. b) Deposition function evolution for the dynamic method.

5.3 Results

5.3.1 GEM

To simulate charging-up in GEMs, we used the constant and the dynamic method simultaneously. In this way, we could compare both methods for the same conditions.

The comparison between methods is shown in fig. 5.8a and 5.8b. This plot represents the sum of all electric charges (the integral of the deposition histograms in fig.5.3a and 5.3b) , per primary avalanche and per hole, deposited in the insulator surface, along the avalanches, for both constant and dynamical step methods.

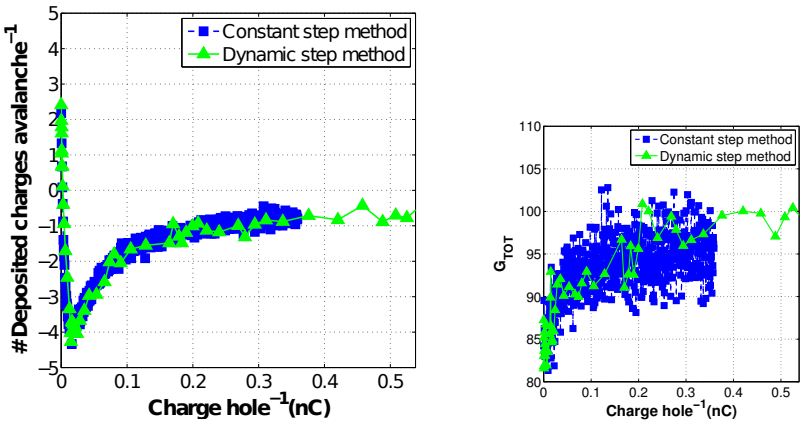

(a) (b)

Figure 5.8: a) Total number of deposited charges per avalanche, for constant and dynamical method. b) Comparison of the absolute gain, along avalanches, between the constant and dynamical method. Dynamical method uses less iterations, saving computational time.

The evolution of the number of deposited charges matches between both methods, but the dynamical method needs less iterations, being faster. Another advantage of the dynamical method is that we don't need to previously know the best initial step of the deposition function. We can start with a very small step and the method will converge to the expected function.

The total gain variation evolution is also compared between methods in figure 5.8b. We observe an increase of the total gain, followed by a stabilization plateau, reached in both methods.

5.3.2 Effective gain dependence with charging-up

The dependence of effective gain with applied voltages between electrodes in the GEM detector, for the situations with and without charging-up, is shown in fig. 5.9a. Two curves are shown, one for simulations assuming no charging-up and the other considering that effect. We observe a gain increase, for charged GEM, of the order of 10-15%. The magnitude of the effect appear to be independent of the applied potential, at least for the considered range of potentials.

5.3.3 Electron transmission dependence with charging-up

During the drift of the primary electrons, these charges can be collected in the top electrodes of the GEM, and will not enter the holes to produce avalanches. The fraction between the number of primary electrons that enter the holes and the total number of primary electrons simulated is defined as the electron transmission. The dependence with charging-up is shown in Fig.5.9b, for various values of V_{GEM}. Transmission equal to 1 mean that all the primary electrons will enter the hole. For lower values of V_{GEM},

the transparency decreases with the charging-up, but for higher values, that dependence will gradually disappear, since transparency will tend to be 1 in both situations.

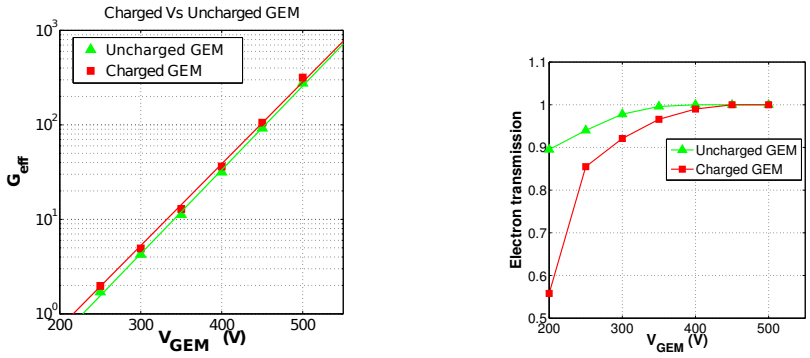

(a) (b)

Figure 5.9: a) Effective gain (number of collected electrons in collection plane by primary avalanche) comparison between charged (red) and uncharged (green) GEM. b) Primary electrons transmission dependence with charging-up. For higher values of V_{GEM} the transmission is not particullary affected.

5.3.4 Electric field variation with charging-up

The variation in the intensity of local electric field in the GEM is represented in Fig 5.10.

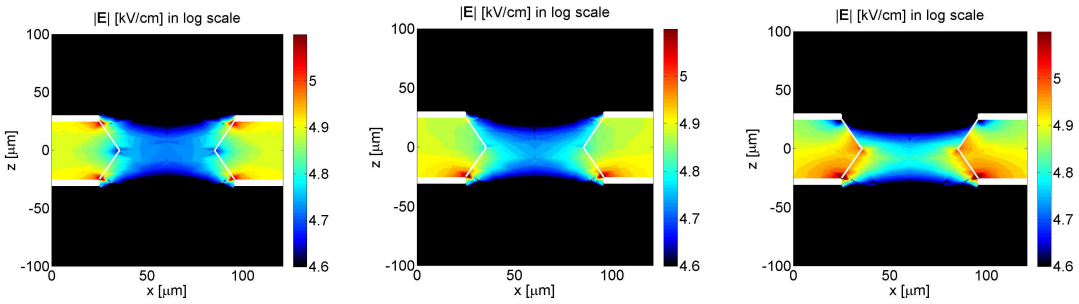

(a) (b) (c)

Figure 5.10: Evolution of the intensity of the electric field, in a GEM cross section, for a) without charging-up, b) after 3 $\times 10^6$ avalanches and c) after 10 $\times 10^6$ avalanches.. Computed with Ansys. Colorbar refers to logarithm of $|\vec{E}|$. Only intensities above $e^{4.6} \simeq 100$ kVcm^{-1} are colored.

The biggest change in the electric field occurs near the electrodes and the hole. While the intensity in the electric field near the top (positive polarized) electrode will decrease, it increases near the center of the hole and the bottom (negative polarized) electrode, where the majority of the avalanches occur, explaining the increase in the gain.

5.3.5 Comparing with experimental measurements

Comparing with experimental measurements of a single GEM, at V_{GEM}=380 V, and with a mixture Argon 70% CO_2 30%, at standard pressure and temperature, is

shown in Fig 5.11. Both experimental and simulated absolute gain initially increases, reaching a plateau. On the other hand, the absolute value of the gain still does not match the simulation and measurements results.

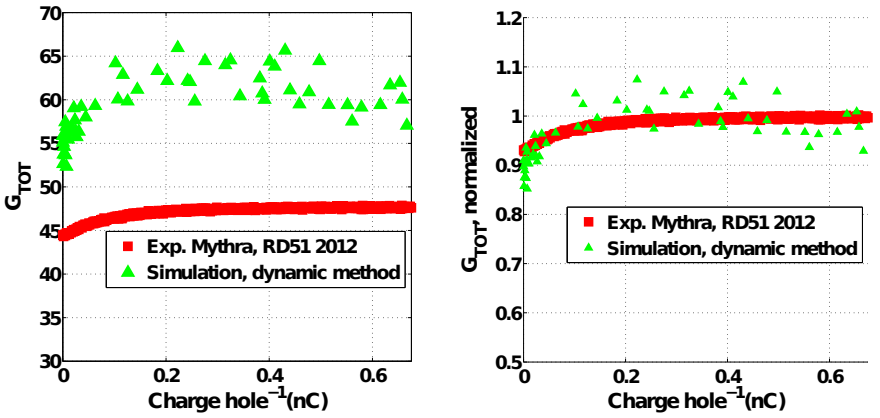

(a) (b)

Figure 5.11: a) Absolute gain comparison between measuremments (red) and simulated (green) results, with V_{GEM}=380 V. b) Same plot as a) but with gain normalized. Experimental data taken by Mythra Nemallapudi at RD51 facilities, CERN.

5.3.6 THGEM

In the case of THGEM, we used the dynamical simulation method since it shows similar results compared with the constant step method, but is considerable faster. The deposition distribution of charges in the insulator surface is different from the one observed in the case of GEM, reflecting the different geometries of the two devices.

The application of the dynamical method to THGEM is presented in fig. 5.12a. The fast variation in the number of deposited charges per avalanche in the earlier iterations, followed by a plateau around zero, is observed, meaning that electrons and ions are compensating each other for later iterations. A variation in the effective gain, for ΔV_{THGEM} =720V is plotted in fig. 5.12b, where we can see a stabilization for the effective gain. In these particular configurations, the effective gain decrease with *charging-up*.

The effective gain variation as a function of V_{THGEM} is plotted in figure 5.13. The magnitude difference between the gain in charged and uncharged THGEM is about 37%, significantly higher than the difference observed in GEMs. The decrease in the gain is observed for all the simulated potentials.

5.4 Simulation of rim influence for charging-up and gas gain

The electric field in MPGDs can change abruptly due to geometric variations between different MPGDs. Particularly, in THGEMs, the rim influence in the gains has not yet been fully understood. In order to study the effect of the rim for the gain, all

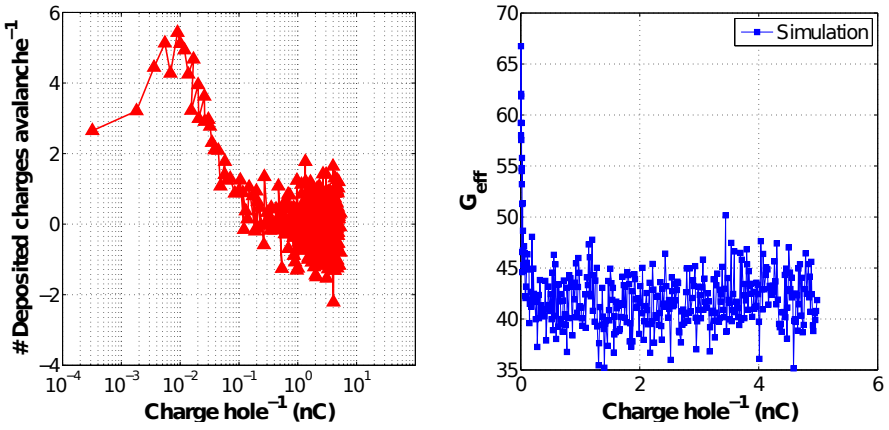

(a) (b)

Figure 5.12: a) Evolution of the total number of deposited charges in insulator, per avalanche, in a THGEM detector, simulated with dynamical method. Log scale is used to show initial increase of positive deposition. b) Evolution of effective gain for ΔV_{THGEM} =720V. We can observe a decrease in effective gain, followed by a stabilization plateau.

---

the dimensions of the THGEM were kept constant, but the rim was changed. For each value of rim, the gain was calculated. Voltage of 600 V between electrodes was used. Results are shown in fig. 5.14a.

The increase of the rim decreases the effective gain. This can be understood if we analyse the electric field. Larger rims will lead to a holes in the metal electrodes, so the density of field lines in the holes will decrease, justifying by lower local electric field, and a gain loss.

Nevertheless, it is usual to observe experimental results where the increase of the rim leads to higher gains. From the experimental point of view, this is related to the fact that larger rims will decrease the spark probability, allowing the application of higher voltages and consequently higher gains. In the simulations we are not taking into account the sparks, so this results shows that for the same voltages, the increase in the rim decreases the gain.

5.5 Simulation of insulator thickness influence in gain in THGEM

Another interesting geometric parameter in MPGDs is the influence of the thickness of the insulator in the gain.

During the fabrication process, defects can be introduced in the geometry of the detector, and for large area detectors, the insulator thickness is one of the parameters that is more likely to be non-uniform. This non-uniformity will cause a local variation in the gain, and depending on this variation, experimental measurements can be significantly affected. In order to study the influence of the insulator thickness in the gain, we simulate the THGEM described in subsection 2.4.2, changing the insulator thickness up to 10% of its designed value. Results are shown in Fig.5.14b, for different values of the rim.

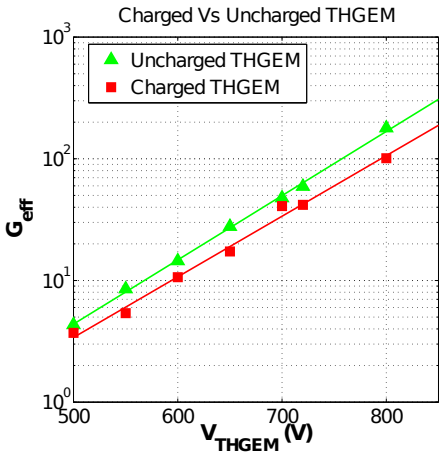

Figure 5.13: Effective gain comparison between charged (red) and uncharged (green) THGEM, for different voltage between electrodes. In opposite with GEM, the charging-up in THGEM decreased the effective gain.

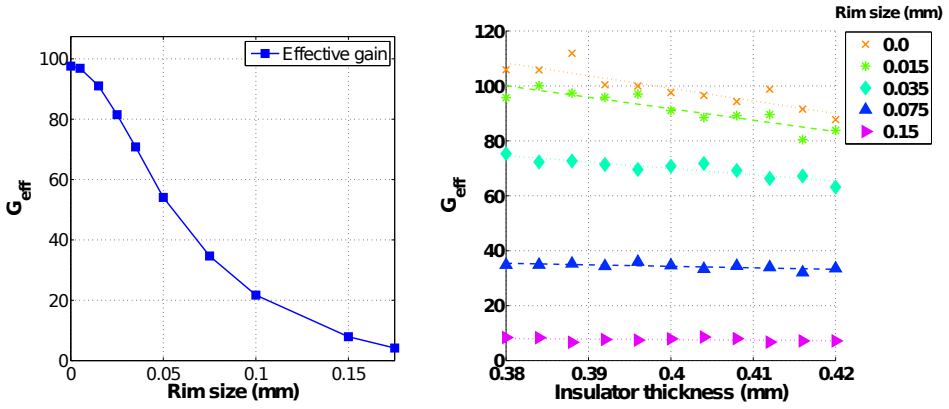

(a) (b)

Figure 5.14: a) Rim influence in the THGEM gain. Higher rims decrease the effective gain. b) Thickness variation influence for the THGEM gain, for different rims. Thick insulator translates in smaller effective gains.

The gain decreases with the increase of the thickness of the insulator. A thinner insulator reduces the distance between electrodes and increase the local electric field, justifying the obtained higher gains.

Higher absolute gain variations due to thickness variation of the insulator appear for higher gains where the maximum gain variation obtained was about $\simeq 20\%$, meaning that this effect can be more important at high amplification stages and for high-precision applications.

Chapter 6

Experimental gain measurements in THGEM

The development of a simple detector to measure the charging-up in THGEMs was one of our goals during this research. For the measurements, we used a gas chamber, filled with a mixture of Neon/Methane (95% Ne-5%CH4), in constant gas flow.

The measurements of the charging-up have proved to be not so simple as the measurements of the detector gain. We have to consider that turning on the voltages in the detector will change the distribution of charges in the insulator material of the THGEM. To avoid that, all the measurements were performed some hours after the voltages had been applied.

Although our gas mixture is assumed to be free of impurities, the use of a kapton window in the detector can allow the entrance of some humidity to the gas chamber, changing the resistivity of the insulator. To avoid this, the detector was heated at 70° C during some hours and left for cool down at room temperature before the measurements.

Finally, to calculate the gain it is mandatory to irradiate the detector, which will induce the charging-up and change the gain, so the measure itself affects the gain, and we need to be very meticulous during the measurements.

6.1 Dimensions and irradiation

A single THGEM with 30 x 30 mm^2 was used, with 0.4 mm of thickness, 0.8 mm of pitch, 0.4 mm of hole diameter and 0.12 mm of rim size (for reference see fig. 2.6b).

The detector vessel was made of aluminium, a Kapton window was used for irradiation. The interior of the detector, where the THGEM is assembled, is shown in Fig. 6.1a.

For the irradiation, we used a Molybdenum X-rays tube, collimated by a 2 mm diameter hole in a 2 mm thick lead plate. This collimation allowed the irradiation of $\sim$ 20 holes in the THGEM due to the x-rays divergence.

An energy histogram is shown in fig. 6.2. For energy calibration of the channels, we used a ^{55}Fe X-ray source of 5.9 keV. After the calibration, we could see that the histogram peak lies at about 10 keV. For gain calculation, we assume that this is the

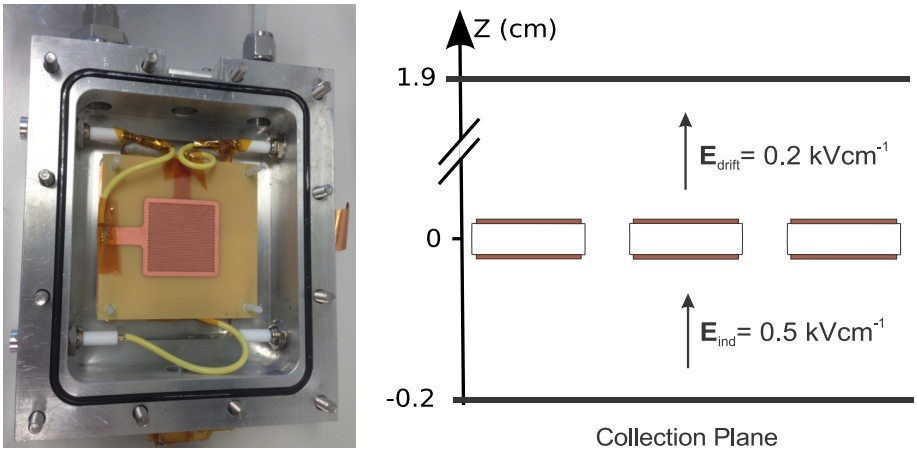

(a) (b)

Figure 6.1: a) Top view of the developed detector, with an assembled THGEM. b) Schematics of the distances between planes and electric fields used in the detector.

---

energy of all the interacting photons in the detector, which is true if we considerer an average value, and fits our propose for the charging-up measurements.

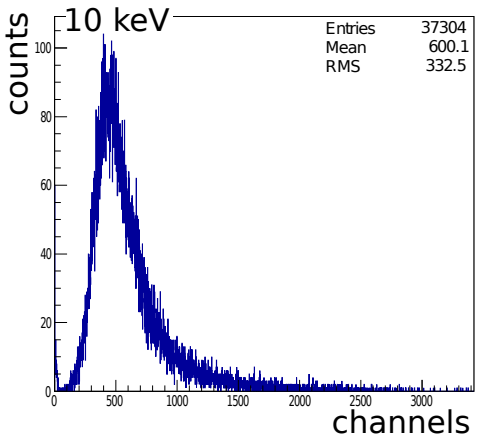

Figure 6.2: Example of the energy histogram of a pulse. The peak was calibrated and lies at 10 keV.

6.2 Electronics

For the analysis of the signal originated by the interaction of the photons in the gas media, we used the diagram described in fig. 6.3. The analogue pulses originated in the detector are amplified by a preamplifier Camberra 2006[52], and converted to digital signals by a analog-digital converter (ADC) digitizer model CAEN V1724[53] of 14 bits.

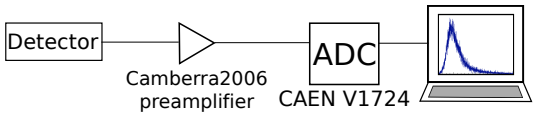

Figure 6.3: Diagram of the steps used for acquisition and analysis of the signals.

6.3 Results

The detector was irradiated with a constant rate during some hours. To measure the gain, over the time, we fit a Gaussian distribution around the peak of the energy histogram obtained during 5 seconds. The position of the peak changes during the time, reflecting the gain variation of the detector.

To calibrate the gain of the detector, we injected a pulse of a known charge into the preamplifier, using a precision capacitor and a pulse generator, and recorded which channel was activated. In this way we can determine the charge correspondent to the fitted peak and use it to calculate the detector gain, over the time.

The results are shown in Fig. 6.4a. During the first minutes of irradiation, we observed a fast decrease in the gain. This is consistent with what we observed in the simulations, as shown in Fig. 6.4b. On the other hand, after some time the gain start to increase, a behaviour that was not observed in simulations. This was already observed by other authors, and the origin of this increase is not yet known. The gain increases continuously until a spark occurs, changing the distribution of charges in the hole surface. Successive sparks occurs after the first, preventing the gain to recover. This suggests that when a spark occurs in the detector, the distribution of charges is also affected, and a concise measurement of the charging-up is no longer possible.

In the Fig. 6.4b, both experimental and simulated effective gain were normalized to the maximum value in order to be compared. For $V_{THGEM} = 720$ V, the experimental gain obtained for Ne-CH4 (95%-5%) mixture ($\simeq 10^4$) is in agreement with other authors[49]. Nevertheless, the simulated effective gain is considerably small ($\simeq 10^2$). This may be related to the simulation software. As reported in [47], especially for higher gains, experimental gain in THGEMs can be some orders of magnitude higher than the simulated values.

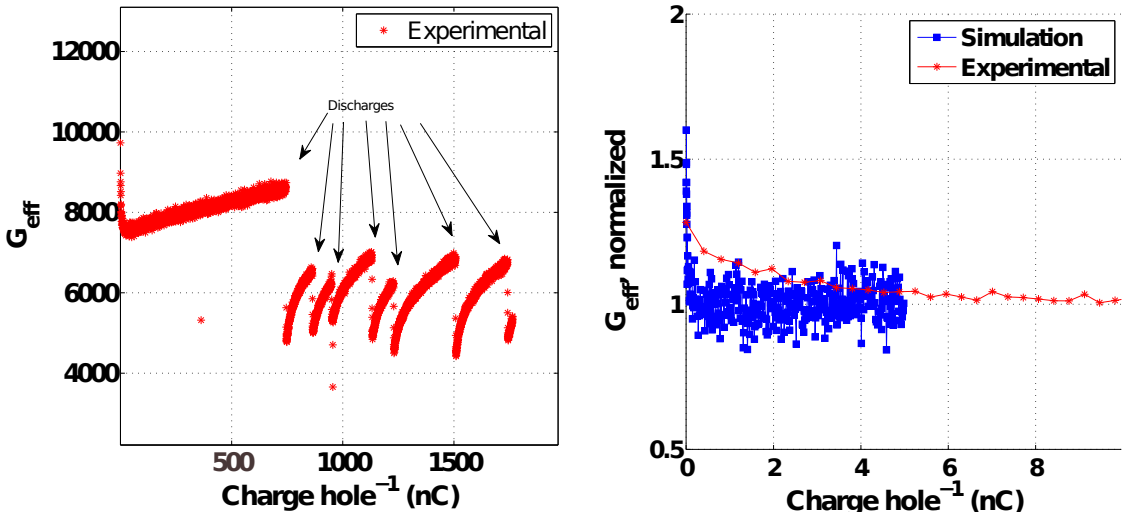

(a) (b)

Figure 6.4: a) Measurements of the THGEM gain variation over the time, normalized to the total charge per hole. b) Comparison between experimental and simulated gain variation for the firsts instants of a).

Chapter 7

Gaseous Compton Camera

The use of the Compton scattering process as an imaging technique was introduced in 1973 in the field of γ-ray astronomy field[54], spreading to other fields such as medical imaging, during the following years [55, 56, 57]

The conventional imaging system in nuclear medicine is the Anger camera, which uses heavy mechanical collimators to resolve the photon spatial distribution. The use of such collimators implies a decrease of sensitivity, i.e. the number of photons that reach the detector[58] creating a trade-off between spatial resolution and doses applied to patients. This limitation can be avoided by using electronic collimation, i.e., using the information from the Compton scattering process[55].

7.1 Geometry of the detector

The simulated detector has a gas vessel with 200 mm of diameter and 69 mm of height. A pressure of 10 bar and several gases and gas mixtures were considered during the simulations. In a common Compton camera, when a incident photon interacts through Compton scattering, part of its energy is transferred to an electron, the recoil electron. We consider that this interaction will occur at a given position (x_0, y_0, z_0) and at a given time t_0. If the energy of the incident and scattered photons are E_{inc} and E_{scatt}, respectively, the kinetic energy of the electron is $E_0 = E_{inc} - E_{scatt}$.

The scattered photon can be absorbed by photoelectric effect, in the position (x_1, y_1, z_1) and a time t_1, producing another electron, called the photo-electron, with energy $E_1 = E_{scatt}$.[5].

Knowing the position of the interactions and the energy deposited in both Compton and photoelectric interactions, we can calculate the scattering angle θ of the incident photon, using Eq. 2.2. This information about θ allow us to define a cone surface with all the possible trajectories of the incident photon, where the vertex of the cone is the position of the Compton interaction (x_0, y_0, z_0), the aperture of the cone is the scattering angle θ and the cone axis is the direction defined between the two interaction positions, as represented in Fig. 7.1a. The intersection of a large number of cones will determine the position of the radiation source. Discrimination between the Compton interactions and the other γ interactions is made using the method described in Refs. [59, 60].

The usual Compton cameras are built using 2 detectors, the *scatterer* and the

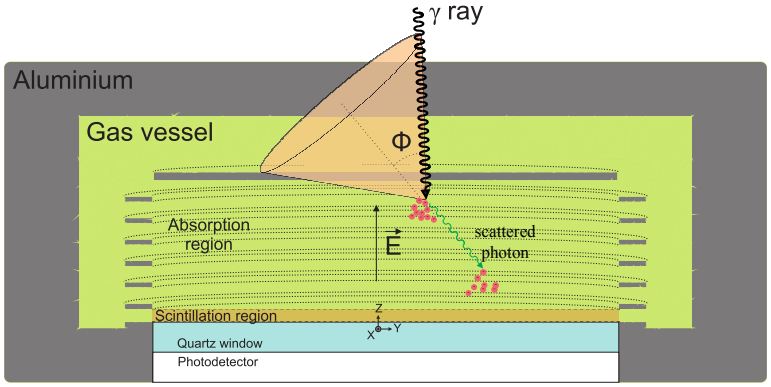

(a)

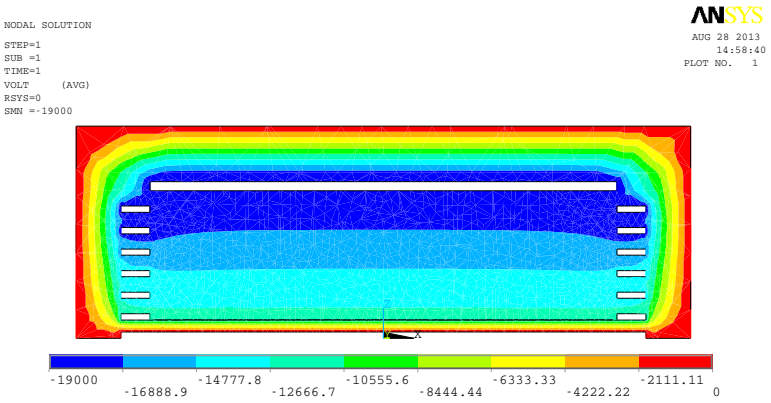

(b)

Figure 7.1: a) Scheme of the Compton Camera studied in this work. The scatterer and the absorber are the gaseous chamber, and a scintillation stage is included to amplify the signal. b) Contour of the potential simulation in the detector.

absorber, made of different materials. Si detectors are widely used for the scatterer, manly due to the lower Doppler broadening effect, while Ge or NaI are mostly used for the absorber due to the higher detection efficiency and reasonable energy resolution for moderate X and γ rays energy. The main problem with such materials are the large area requirements for detection and the high costs associated.

In this study we propose a gaseous chamber, filled with pure noble gases (or mixtures), which can act as a scatter and absorber stages in the same medium. The gas volume is divided into two regions, the drift or absorption region, where Compton and photoelectric interaction will occur, and the scintillation region, where the produced charge will be amplified through electroluminescence process.

The position and energy measurements will be performed in a large-area gaseous photomultiplier with position discrimination capability.

7.1.1 Absorption/Drift region

After the Compton interaction, the kinetic energy of the recoil electron E_0 is transferred to the gas media through consecutive collisions. Depending in the collisions mechanisms, excitations and ionisations can occur leading to the production of a primary electron cloud.

The number of electrons in the cloud is proportional to the energy of the primary electron, E_0. Excitations will produce primary scintillation. This primary scintillation can be detected and used as a trigger for timing.

An electric field of 0.2 $kVcm^{-1}Torr^{-1}$ (bellow the excitation threshold) applied in this region will force the electron cloud to drift through the gas, from the absorption region until the scintillation region. This electron drift is performed at constant velocity, and the depth of interaction position (z) along the drift region can be determine by knowing that the arriving time of the electron cloud to the end of the drift region is proportional to the drift length.

7.1.2 Scintillation region

The scintillation region, placed just after the drift region, is created in the gas by positioning two parallel grids, separated by 4 mm and applying an electric field above the gas excitation threshold.

After the electron clouds drift from the drift region into the scintillation region, the high electric field (4 $kVcm^{-1}Torr^{-1}$, above the excitation threshold of the considered gases) will accelerate the electrons between collisions, which gain enough energy to excite the gas, producing electroluminescence light. Each photon is emitted in a 4π solid angle direction, with equal probability for all directions. A readout system below the scintillation region is used to detect part of the produced photons coming from the scintillation region, as well as the primary scintillation used for trigger the starting time. A photo-sensor composed by CsI and a THCOBRA detector is in test for our prototype readout.

The determination of the centroid of all the detected photons in the photo-sensor will give the 2D position (x,y) of each electron cloud. The third coordinate (z) of the Compton or photoelectric interaction will be calculated through the measured time between primary scintillation and secondary scintillation, by knowing the electron drift velocity in the gas.

7.2 Drift simulations of primary charges

At this stage, only the drift of the primary electron cloud was simulated, neglecting if the electrons were originated by Compton or photoelectric interaction. Our interest is centred in the study of the electron cloud drift velocity for different gases and the number of collected photons at the photo-sensor.

7.2.1 Drift velocity for different gas mixtures

We first considered a set of 100 primary electrons, starting their drift at (0,0,z), where z is the variable depth of interaction in the absorption region, with random velocity direction and starting energy equal to 0 eV. After the drift of the electrons, the position (x,y) of the secondary scintillation photons in the photo-sensor and the drifting time of each electron in the absorption region are recorded. The drifting time will allow to construct a calibration function of the interaction depth as a function of

the drifting time of the electrons. The centroid position of the 2D histograms for the detected photons will give the interaction position (x,y) in the absorption region.

The results of the depth of interaction as a function of the drifting time is shown in Fig. 7.2 for different noble gases and mixtures, where the distance, in cm, is the vertical distance between the starting drifting point of the electrons and the top grid of the scintillation region.

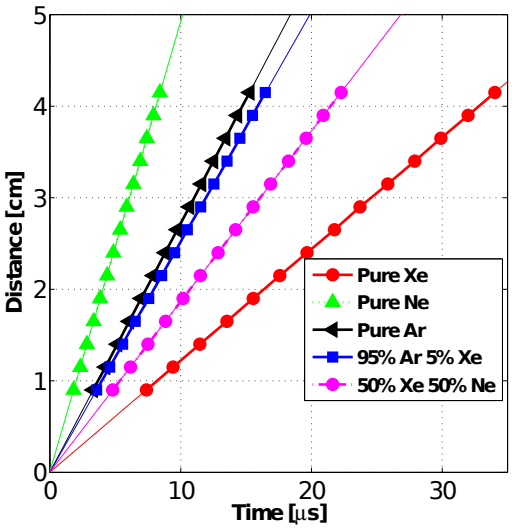

Figure 7.2: Vertical distance travelled by drifting electrons, as a function of drifting time, for different gases/mixtures, and for an electric field 0.2 $kVcm^{-1}Torr^{-1}$.

We can observe that Xenon is the gas presenting the lowest drift velocity, thus defining the highest dead time of the detector (minimum time for discrimination between two different events). On the other side, Neon offers the highest drift velocity. Nevertheless, as described in [61], the best gas choice is Xenon or a mixture of 95% Argon and 5% Xenon, if the detector dead time is not a problem, because these mixtures shows lower Doppler broadening. If the dead time is mandatory, i.e., high absorption rates, Ne will be the best option being detection efficiency strongly limited.

7.2.2 Scintillation production and photon detection

Again, an initial set of 100 primary electrons were simulated, starting their drift at a given value of z. Inside the scintillation region, electrons will collide and excite the gas particles.

After some time, these electrons will be collected at the bottom grid located below the scintillation region. The emission of the scintillation photons is an isotropic random process.

Part of the photons will cross through a quartz glass window, being collected by a photo-sensor located after the window. For the propose of the simulation, the photo sensor was defined as a plane with 10x10 cm^2 as detection area, located 3.6 cm bellow the bottom grid of the scintillation region, defining the detection solid angle.

A two-dimensional histogram of all the collected photons in the photo-sensor is presented in Fig. 7.3a and 7.3b. A very thin peak is observed, which is used to calculate

the centroid of the histogram for each cluster of the 100 primary electrons considered (corresponding to a few keV of deposited energy). The centroid gives information of the initial position (x,y) of the drifting electrons, i.e. the two spatial coordinates of the Compton interaction in the absorption region.

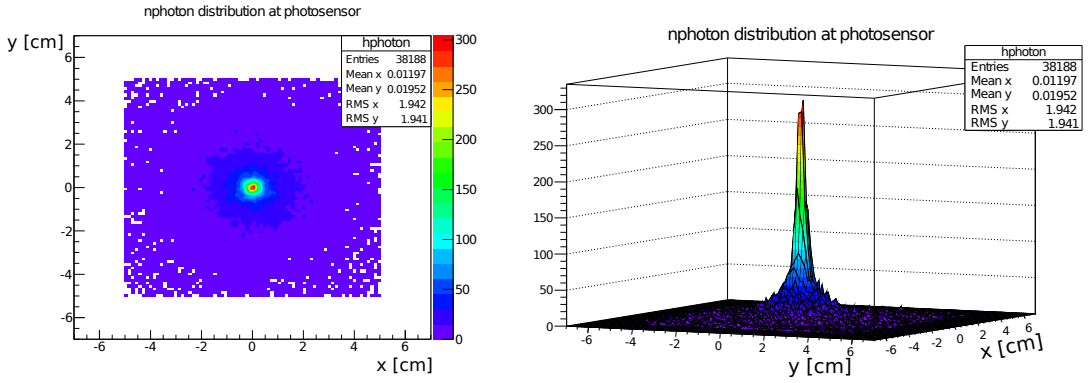

(a) (b)

Figure 7.3: Histogram representation at a) 2-dimensions and b) 3-dimensions of the detected photons in the photo sensor, for 100 primary drifting electrons, starting the drift at the (0,0,4) cm, drifting in pure Xenon at 7500 Torr and 293 K.

A table with the number of detected photons, per primary electron, and the comparison between the initial position of the primary electrons and the calculated centroid position for different gases, is shown in Tab. 7.1.

Gas	Y_{VUV} (photons electron^{-1} cm^{-1} Torr^{-1})	Photon centroid	
		X (mm)	Y (mm)
Xenon	0.485 ± 0.001	0.10 ± 0.007	-0.04 ± 0.07
Neon	4.5 ± 0.6	-0.40 ± 0.002	-0.07 ± 0.02
Argon	0.320 ± 0.002	0.036 ± 0.007	-0.052 ± 0.07

Table 7.1: Electroluminescence yield calculated using 100 primary electrons drifting from the initial position (0,0,4) cm. The position of the centroid of detected photons in the photosensor are also shown. Difference between initial position of electron cloud and photon centroid calculation is less than 1 mm for the analised gases. Simulated with an electric field of 4 kVcm^{-1}Torr^{-1}.

The calculated values for Y_{VUV} are consistent with the references(e.g. [62, 63]), except for Neon, where the obtained Y_{VUV} is higher. The simulated scintillation electric field (4 kVcm^{-1} Torr^{-1}) is above the ionization threshold in Neon ($\sim$ 2.3 kVcm^{-1}Torr^{-1}), proving that some secondary charges are produced, which in turn will produce more scintillation, increasing Y_{VUV}. Note that we defined the Y_{VUV} per primary electron, and not per total number of electrons producing scintillation.

7.3 Image reconstruction

As mentioned before, for the Compton image reconstruction we need to determine the position of interaction and the energy of both recoil electron and scattered photon in the gas From the time difference between primary and secondary scintillation signals, we can calculate the distance travelled by the primary electron clouds by using the simulated drift time data, obtaining the vertical depth of each interaction.

Knowing the position (x,y,z) and the energy deposited in each interaction, we can use Eq. 2.2 to calculate a cone surface of possible directions for the incoming interacting photon. The superposition of a large number of cones (meaning large number of statistic events) will enhance a region where a large number of surfaces intercept one another and this region is the source of the radiation. An illustrative example is in Fig. 7.4a and 7.4b.

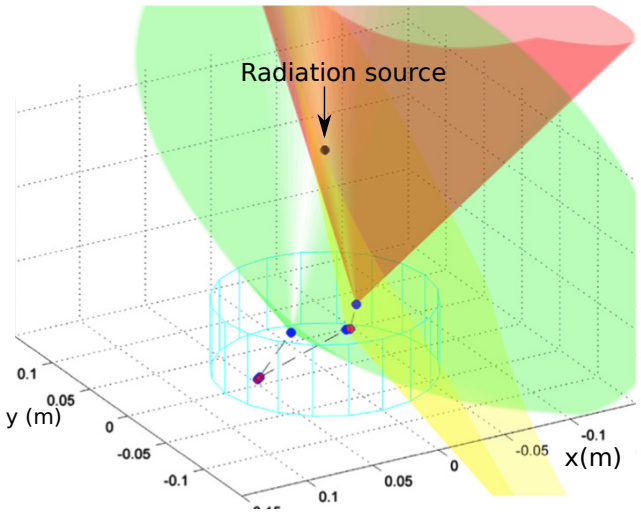

(a)

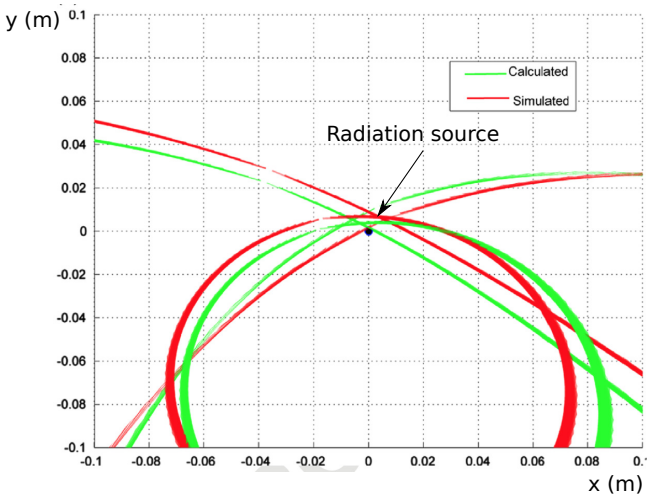

(b)

Figure 7.4: a) Representation of three Compton events and the correspondent cone surfaces. The point of interception of the three surfaces is the calculated position of the radiation source. b) A two dimensional projection of a).

Chapter 8

Conclusions and future work

Simulation of the drift of charged particles in gas were made during this work. Studies were applied for two types of gaseous detectors, the MPGDs and a specific gaseous γ-Camera, called a Compton Camera.

For the MPGDs, we studied in particular the GEMs and THGEMs. A study of the charging-up effect in the insulator of this detectors was made. We introduce two simulation algorithms to simulate charging-up in MPGDs. The method is not limited to GEMs and THGEMs and can be extrapolated to other MPGDs that in theory suffer insulator charging-up.

Our results showed that charging-up increase the gain measured for GEMs, being in concordance with experimental data taken from other authors. The order of magnitude between simulated and experimental gain is again in concordance. We also saw that the charging-up in GEMs do not affect the transparency of the detector for higher gains.

For THGEM, we saw in our simulations a decrease in the gain, followed by a stabilization plateau. The experimental measurement of the charging-up in our laboratory revealed this initial decrease in the gain, but after some time the tendency inverts and the gain start to slowly increase until the detector suffer sparks and the measure became compromised after that. Nevertheless, simulated gain is about 2 orders of magnitude lower than experimental gain. This was observed by other authors for THGEMS at high gain operation, and is likely to be a software issue and agreement between experimental and simulated gain is still missing. For THGEMs, we also simulated the influence of some geometric parameters in the gain of the detector. First, we simulate the effect of the thickness of the insulator and we observe that thinner insulators lead to higher gains. The size of the rim was also studied, revealing that larger rims decrease the detector gain for the same applied voltage. This topic is very important since the rim in THGEM was introduced to reduce sparks in the detector, and larger rims allow higher applied voltages and consequently higher gains. What we conclude is that, for the same potential, a larger rim decreases the gain, but higher voltages can be reach.

For the Compton camera, a new concept with electronic collimator and a gas filled chamber is presented. First, we simulate the electric field configuration of the detector. The simulation of electron drift in different gases show that Neon should be the best option to fill the gas camera, because it shows the higher drift velocity for electrons, reducing the dead time of the detector. However, Xenon or a mixture 95% Argon

5% Xenon will be used because they show better performances considering Doppler broadening effect and detection efficiency.

The determination of the centroid of the detected scintillation photons in the photosensor shows a difference between expected and calculated 2D position with an error less than 1 mm, for each direction, allowing the determination of a submilimetric γ photon interaction position.

The scintillation yields calculated for different gases are in agreement with other authors.

As a future work, we want to include the simulation of the mobility of deposited charges in the insulator surfaces in the charging-up problem. This could help to explain the increase in the gain observed in THGEM measurements. The application of the method to other MPGDs can also be done in the future, since the method is not limited to the studied cases.

The use of a new software for electric calculations, called Nearly Exact Boundary Element Method (neBEM) is also being considered, since it shows better precision in the calculations compared with Finite Element Methods software (like Ansys, used for this work).

For the Compton Camera we intend to perform a complete simulation of the detector response in terms of spatial position and energy determination, considering all the physical phenomena for different applied voltages, pressures and filling gases.

Bibliography

[1] R. I. Frankel, "Centennial of röntgen's discovery of x-rays," *Western Journal of Medicine*, vol. 164, no. 6, pp. 497–501, 1996.

[2] L. Badash, "Becquerel's blunder," *SOCIAL RESEARCH*, vol. 72, pp. 31–62, SPR 2005.

[3] `http://www.nobelprize.org/nobel_prizes/physics/laureates/1906/`, Last visited 12 October 2013, pdf available .

[4] `http://www.nobelprize.org/nobel_prizes/physics/laureates/1936/hess-bio.html`, Last visited 12 October 2013, pdf available .

[5] G. F. Knoll, *Radiation Detection and Measurements, third edition*. John Wiley & Sons, Inc., 3rd ed., 1999.

[6] `http://www.nobelprize.org/nobel_prizes/physics/laureates/1992/charpak-facts.html`, Last visited 12 October 2013, pdf available .

[7] A. Oed, "Position-sensitive detector with microstrip anode for electron multiplication with gases," *NIMA*, vol. 263, no. 23, pp. 351 – 359, 1988.

[8] Y. Giomataris, P. Rebourgeard, J. Robert, and G. Charpak, "Micromegas: a high-granularity position-sensitive gaseous detector for high particle-flux environments," *NIMA*, vol. 376, no. 1, pp. 29 – 35, 1996.

[9] F. Sauli, "Gem: A new concept for electron amplification in gas detectors," *NIMA*, vol. 386, no. 2-3, pp. 531 – 534, 1997.

[10] C. Shalem, R. Chechik, A. Breskin, and K. Michaeli, "Advances in thick gem-like gaseous electron multiplier part i: atmospheric pressure operation," *NIMA*, vol. 558, no. 2, pp. 475 – 489, 2006.

[11] J. Maia, J. Veloso, J. dos Santos, A. Breskin, R. Chechik, and D. Mörmann, "Advances in the micro-hole and strip plate gaseous detector," *NIMA*, vol. 504, no. 13, pp. 364 – 368, 2003.

[12] M. Chefdeville, P. Colas, Y. Giomataris, H. van der Graaf, E. Heijne, S. van der Putten, C. Salm, J. Schmitz, S. Smits, J. Timmermans, and J. Visschers, "An electron-multiplying micromegas grid made in silicon wafer post-processing technology," *NIMA*, vol. 556, no. 2, pp. 490 – 494, 2006.

[13] M. N. Wernick and J. N. Aarsvold, *Emission Tomography - The Fundamentals of PET and SPECT*. Elsevier, 2004.

[14] H. G. Compton, "The spectrum of scattered x rays," *Phys. Rev.*, vol. 22, no. 5, p. 409, 1923.

[15] W. Blum, W. Riegler, and L. Rolandi, *Particle Detection with Drift Chambers*. Springer, 2nd ed., 2008.

[16] L. G. H. Huxley, R. W. Crompton, and M. T. Elford, "Use of the parameter e/n," *British Journal of Applied Physics*, vol. 17, no. 9, p. 1237, 1966.

[17] F. Penning, "The starting potential of the glow discharge in neon argon mixtures between large parallel plates: Ii. discussion of the ionisation and excitation by electrons and metastable atoms," *Physica*, vol. 1, no. 712, pp. 1028 – 1044, 1934.

[18] M. J. Druyvesteyn and F. M. Penning, "The mechanism of electrical discharges in gases of low pressure," *Rev. Mod. Phys.*, vol. 12, pp. 87–174, Apr 1940.

[19] J. M. F. dos Santos, J. A. M. Lopes, J. F. C. A. Veloso, P. C. P. S. Simões, T. H. V. T. Dias, F. P. Santos, P. J. B. M. Rachinhas, L. F. Requicha Ferreira, and C. A. N. Conde, "Development of portable gas proportional scintillation counters for x-ray spectrometry," *X-Ray Spectrometry*, vol. 30, no. 6, pp. 373–381, 2001.

[20] V. Peskov, "Progress in micro-pattern gaseous detectors and their applications," *Advances in sensors and Interfaces, 2009. IWASI 2009. 3rd International Workshop on*, pp. 52–57, 2009.

[21] C. Monteiro, A. Conceio, F. Amaro, J. Maia, A. Bento, L. Ferreira, J. Veloso, J. dos Santos, A. Breskin, and R. Chechik, "Secondary scintillation yield from gaseous micropattern electron multipliers in direct dark matter detection," *Physics Letters B*, vol. 677, no. 3-4, pp. 133 – 138, 2009.

[22] S. R. Elliott and J. Engel, "Double-beta decay," *Journal of Physics G: Nuclear and Particle Physics*, vol. 30, no. 9, p. R183, 2004.

[23] K. Mehta, "The theory and test results of gem foils and the korean gem detector respectively." `http://indico.cern.ch/getFile.py/access?resId=3&materialId=slides&confId=145233`, October, 2011.

[24] "Gas detectors development group." `http://gdd.web.cern.ch/GDD/`. last checked: 05.06.2013.

[25] I. I. Sobelman and J. Toennis, *Atomic spectra and radiative transitions*. Springer-Verlag, 2nd ed., 1992.

[26] E. Aprile, A. E. Bolotnikov, A. I. Bolozdynya, and T. Doke, *Noble Gas Detectors*. Wiley-VCH, 2006.

[27] M. Suzuki and S. Kubota, "Mechanism of proportional scintillation in argon, krypton and xenon," *Nucl.Instrum.Meth.*, vol. 164, pp. 197–199, 1979.

[28] R. E. Packard, F. Reif, and C. M. Surko, "Ultraviolet emission spectra of electron-excited solid and liquid neon," *Phys. Rev. Lett.*, vol. 25, pp. 1435–1439, Nov 1970.

[29] Y. Tanaka, "Continuous emission spectra of rare gases in the vacuum ultraviolet region," *J. Opt. Soc. Am.*, vol. 45, pp. 710–713, Sep 1955.

[30] Y. Tanaka, A. S. Jursa, and F. J. Leblanc, "Continuous emission spectra of rare gases in the vacuum ultraviolet

region. ii. neon and helium," *J. Opt. Soc. Am.*, vol. 48, pp. 304–307, May 1958.
[31] A. Morozov, T. Heindl, R. Krucken, A. Ulrich, and J. Wieser, "Conversion efficiencies of electron beam energy to vacuum ultraviolet light for ne, ar, kr, and xe excited with continuous electron beams," *Journal of Applied Physics*, vol. 103, no. 10, 2008. cited By (since 1996)15.
[32] C. Oliveira, P. Correia, A. Ferreira, S. Biagi, R. Veenhof, and J. Veloso, "Simulation of gaseous ar and xe electroluminescence in the near infra-red range," *Nuclear Instruments and Methods in Physics Research Section A: Accelerators, Spectrometers, Detectors and Associated Equipment*, vol. 722, no. 0, pp. 1 – 4, 2013.
[33] C. M. B. Monteiro, *Determination of argon and xenon absolute electroluminescence yields in Gas Proportional Scintillation Counter*. PhD thesis, University of Coimbra, 2010.
[34] "Garfield." `http://garfield.web.cern.ch/garfield/`. last checked: 25.05.2013.
[35] "Garfield++." `http://garfieldpp.web.cern.ch/garfieldpp/`. last checked: 02.06.2013.
[36] "Mabtoltz." `http://consult.cern.ch/writeup/magboltz/`. last checked: 02.06.2013.
[37] S. Biagi, "Monte carlo simulation of electron drift and diffusion in counting gases under the influence of electric and magnetic fields," *NIMA*, vol. 421, no. 12, pp. 234 – 240, 1999.
[38] "Root." `http://root.cern.ch/drupal/`. last checked: 25.05.2013.
[39] "Lxcat open-source project, phelps database." `http://www.lxcat.laplace.univ-tlse.fr`. last checked: 02.06.2013.
[40] "Nearly exact boundary element method." `http://www.saha.ac.in/cs/ino.web/neBEM/Solver.html`. last checked: 03.06.2013.
[41] S. K. Mendiratta, *Introdução ao electromagnetismo*. Fundação Calouste Gulbenkian, 2nd ed., 1995.
[42] S. A. Kafafi, "The ionization potential, electron affinity and energy gap of polyimide," *Chemical Physics Letters*, vol. 169, no. 6, pp. 561 – 563, 1990.
[43] G. M. Sessler, B. Hahn, and D. Y. Yoon, "Electrical conduction in polyimide films," *Journal of Applied Physics*, vol. 60, no. 1, pp. 318–326, 1986.
[44] Z. Ziari, S. Sahli, A. Bellel, Y. Segui, and P. Raynaud, "Simulation of surface potential decay of corona char ged polyimide," *Dielectrics and Electrical Insulation, IEEE Transactions on*, vol. 18, no. 5, pp. 1408–1415, 2011.
[45] A. A. Alagiriswamy, K. S. Narayan, and G. Raju, "Relaxation processes in aromatic polyimide," *Journal of Physics D: Applied Physics*, vol. 35, no. 21, p. 2850, 2002.
[46] V. Tikhonov and R. Veenhof, "Gem simulation methods development," *NIMA*, vol. 478, no. 12, pp. 452 – 459, 2002. Proceedings of the ninth Int.Conf. on Instrumentation.
[47] C. A. F. dos Santos, "Simulacção de avalanches de electrões em detectores gasosos de radiação," Master's thesis, University of Aveiro, http://ria.ua.pt/bitstream/10773/2618/1/2009001142.pdf, 2009.
[48] M. Alfonsi, G. Croci, S. D. Pinto, E. Rocco, L. Ropelewski, F. Sauli, R. Veenhof, and M. Villa, "Simulation of the dielectric charging-up effect in a gem detector," *NIMA*, vol. 671, no. 0, pp. 6 – 9, 2012.
[49] M. Cortesi, V. Peskov, G. Bartesaghi, J. Miyamoto, S. Cohen, R. Chechik, J. M. Maia, J. M. F. dos Santos, G. Gambarini, V. Dangendorf, and A. Breskin, "Thgem operation in ne and ne/ch 4," *Journal of Instrumentation*, vol. 4, no. 08, p. P08001, 2009.
[50] Ö. Şahin, I. Tapan, E. N. Özmutlu, and R. Veenhof, "Penning transfer in argon-based gas mixtures," *Journal of Instrumentation*, vol. 5, no. 05, p. P05002, 2010.
[51] S. Dildick, "Gas gain in a single gem: parameter space." `http://garfieldpp.web.cern.ch/garfieldpp/examples/gemgain/SvenDildick_20111123.pdf`, RD51 mini-week, November 2011.
[52] `http://www.canberra.ru/html/products/detectors/preamplifiers/2006.pdf`, Last visited 14 October 2013, pdf available .
[53] `http://www.caen.it/csite/CaenProd.jsp?idmod=483&parent=11`, Last visited 14 October 2013, pdf available .
[54] V. Schönfelder, A. Hirner, and K. Schneider, "A telescope for soft gamma ray astronomy," *Nuclear Instruments and Methods*, vol. 107, no. 2, pp. 385 – 394, 1973.
[55] R. W. Tood, J. M. Nightingale, and D. B. Everett, "A proposed gamma-camera," *Nature*, vol. 251, pp. 132–134, 1974.
[56] J. Martin, G. Knoll, D. Wehe, N. Dogan, V. Jordanov, N. Petrick, and M. Singh, "A ring compton scatter camera for imaging medium energy gamma rays," *Nuclear Science, IEEE Transactions on*, vol. 40, no. 4, pp. 972–978, 1993.
[57] C. J. Solomon and R. J. Ott, "Gamma ray imaging with silicon detectors - a compton camera for radionuclide imaging in medicine," *NIMA*, vol. 273, no. 23, pp. 787 – 792, 1988.
[58] A. D. Guerra and N. Belcari, "State-of-the-art of pet, {SPECT} and {CT} for small animal imaging," *NIMA*, vol. 583, no. 1, pp. 119 – 124, 2007. Proceedings of the 6th International Conference on Radiation Effects on Semiconductor Materials, Detectors and Devices.
[59] A. Bolozdynya, V. Egorov, A. Koutchenkov, G. Safronov, G. Smirnov, S. Medved, and V. Morgunov, "High pressure xenon electronically collimated camera for low energy gamma ray imaging," *Nuclear Science, IEEE Transactions on*, vol. 44, no. 6, pp. 2408–2414, 1997.
[60] H. Bruning, A. Breskin, R. Chechik, V. Dangendorf, A. Demian, K. Ullmann, and H. Schmidt-Bcking, "A large volume 3d imaging gas scintillation counter with csi-based wire chamber readout," *NIMA*, vol. 348, no. 2-3, pp. 223 – 227, 1994.
[61] C. Azevedo, F. Pereira, T. Lopes, P. Correia, A. Silva, L. Carramate, D. Covita, and J. Veloso, "A gaseous compton camera using a 2d-sensitive gaseous photomultiplier for nuclear medical imaging," *NIMA*, no. 0, pp. –, 2013.
[62] C. A. B. de Oliveira, *Monte Carlo study of electroluminescence in gaseous detectors*. PhD thesis, Universidade de Aveiro, 2011.
[63] C. Oliveira, H. Schindler, R. Veenhof, S. Biagi, C. Monteiro, J. dos Santos, A. Ferreira, and J. Veloso, "A simulation toolkit for electroluminescence assessment in rare event experiments," *Physics Letters B*, vol. 703, no. 3, pp. 217 – 222, 2011.